THE MASS–METALLICITY RELATION WITH THE DIRECT METHOD ON STACKED SPECTRA OF SDSS GALAXIES

BRETT H. ANDREWS[1] & PAUL MARTINI[1]
SUBMITTED TO APJ

ABSTRACT

The relation between galaxy stellar mass and gas-phase metallicity is a sensitive diagnostic of the main processes that drive galaxy evolution, namely cosmological gas inflow, metal production in stars, and gas outflow via galactic winds. We employed the direct method to measure the metallicities of ∼200,000 star-forming galaxies from the SDSS that were stacked in bins of (1) stellar mass and (2) both stellar mass and star formation rate (SFR) to significantly enhance the signal-to-noise ratio of the weak [O III] λ4363 and [O II] $\lambda\lambda$7320, 7330 auroral lines required to apply the direct method. These metallicity measurements span three decades in stellar mass from $\log(M_\star/\mathrm{M}_\odot) = 7.4–10.5$, which allows the direct method mass–metallicity relation to simultaneously capture the high-mass turnover and extend a full decade lower in mass than previous studies that employed more uncertain strong line methods. The direct method mass-metallicity relation rises steeply at low mass (O/H $\propto M_\star^{1/2}$) until it turns over at $\log(M_\star/\mathrm{M}_\odot) = 8.9$ and asymptotes to $12 + \log(\mathrm{O/H}) = 8.8$ at high mass. The direct method mass–metallicity relation has a steeper slope, a lower turnover mass, and a factor of two to three greater dependence on SFR than strong line mass–metallicity relations. Furthermore, the SFR-dependence appears monotonic with stellar mass, unlike strong line mass–metallicity relations. We also measure the N/O abundance ratio, an important tracer of star formation history, and find the clear signature of primary and secondary nitrogen enrichment. N/O correlates tightly with oxygen abundance, and even more so with stellar mass.

Keywords: Galaxies: general — Galaxies: abundances — Galaxies: ISM — Galaxies: evolution — Galaxies: stellar content — ISM: abundances

1. INTRODUCTION

Galaxy metallicities are one of the fundamental observational quantities that provide information about their evolution. The metal content of a galaxy is governed by a complex interplay between cosmological gas inflow, metal production by stars, and gas outflow via galactic winds. Inflows dilute the metallicity of a galaxy in the short term but provide the raw fuel for star formation on longer timescales. This gas turns into stars, which convert hydrogen and helium into heavier elements. The newly formed massive stars inject energy and momentum into the gas, driving large-scale outflows that transport gas and metals out of the galaxy. The ejected metals can escape the gravitational potential well of the galaxy to enrich the intergalactic medium or reaccrete onto the galaxy and enrich the inflowing gas. This cycling of baryons in and out of galaxies directly impacts the stellar mass ($M_\star$), metallicity (Z), and star formation rate (SFR) of the galaxies. Thus, the galaxy stellar mass–metallicity relation (MZR) and the stellar mass–metallicity–SFR relation serve as crucial observational constraints for galaxy evolution models that attempt to understand the build up of galaxies across cosmic time. Here we present new measurements of the MZR and the $M_\star$–Z–SFR relation that span three orders of magnitude in stellar mass with metallicities measured with the direct method.

The first indication of a correlation between mass and metallicity came when Lequeux et al. (1979) demonstrated the existence of a relation between total mass and metallicity for irregular and blue compact galaxies. Subsequent studies showed that metallicity also correlates with other galaxy properties, such as luminosity (Rubin et al. 1984) and rotation velocity (Zaritsky et al. 1994; Garnett 2002). The ad-

vent of reliable stellar population synthesis models (Bruzual & Charlot 2003) enabled more accurate stellar mass measurements from spectral energy distributions. Tremonti et al. (2004, hereafter T04) showed the existence of a tight correlation between galaxy stellar mass and metallicity amongst ∼53,000 galaxies from the Sloan Digital Sky Survey (SDSS; York et al. 2000) DR2 (Abazajian et al. 2003) based on the tellar mass measurements from Kauffmann et al. (2003a). The T04 MZR increases as roughly O/H $\propto M_\star^{1/3}$ from $M_\star = 10^{8.5}$–$10^{10.5}$ M$_\odot$ and then flattens above $M_\star \sim 10^{10.5}$ M$_\odot$. They found that the scatter in the MZR was smaller than the scatter in the luminosity–metallicity relation and concluded that the MZR was more physically motivated. Lee et al. (2006) extended the MZR down another ∼2.5 dex in stellar mass with a sample of local dwarf irregular galaxies. The scatter and slope of the Lee et al. (2006) MZR are consistent with the T04 MZR (c.f., Zahid et al. 2012a), but the Lee et al. (2006) MZR is offset to lower metallicities by 0.2–0.3 dex. This offset is likely because T04 and Lee et al. (2006) use different methods to estimate metallicity. Later work by Ellison et al. (2008) discovered that galaxies with high SFRs (and larger half-light radii) are systematically offset to lower metallicities than more weakly star-forming galaxies at the same stellar mass. Mannucci et al. (2010) and Lara-López et al. (2010) studied this effect in a systematic fashion and demonstrated that the scatter in the MZR is reduced further by accounting for SFR. Mannucci et al. (2010) introduced the concept of the fundamental metallicity relation (FMR) by parametrizing the second-order dependence of the MZR on SFR with a new abscissa,

$$\mu_\alpha \equiv \log(M_\star) - \alpha\log(\mathrm{SFR}), \qquad (1)$$

where the coefficient α is chosen to minimize the scatter in the relation. We will refer to this particular parametrization as the FMR but the general relation as the $M_\star$–Z–SFR relation.

[1] Department of Astronomy, The Ohio State University, 140 West 18th Avenue, Columbus, OH 43210, andrews@astronomy.ohio-state.edu

Interestingly, Mannucci et al. (2010) and Lara-López et al. (2010) found that the $M_\star$–Z–SFR relation does not evolve with redshift up to $z \sim 2.5$, as opposed to the MZR (Erb et al. 2006; Maiolino et al. 2008; Zahid et al. 2011; Moustakas et al. 2011). However, this result depends on challenging high redshift metallicity measurements, specifically the Erb et al. (2006) sample of stacked galaxy spectra at $z \sim 2.2$ and the Maiolino et al. (2008) sample of nine galaxies at $z \sim 3.5$.

Galaxy evolution models aim to reproduce various features of the MZR and $M_\star$–Z–SFR relation, specifically their slope, shape, scatter, and evolution. The most distinguishing characteristic of the shape of the MZR is that it appears to flatten and become independent of mass at $M_\star \sim 10^{10.5}$ $M_\odot$. The canonical explanation is that this turnover reflects the efficiency of metal ejection from galaxies because the gravitational potential wells of galaxies at and above this mass scale are too deep for supernova-driven winds to escape (Dekel & Silk 1986; Dekel & Woo 2003; Tremonti et al. 2004). In this scenario, the metallicity of these galaxies approaches the effective yield of the stellar population. However, recent simulations by Oppenheimer & Davé (2006), Finlator & Davé (2008), and Davé et al. (2011a,b) show that winds characterized by a constant velocity and constant mass-loading parameter (mass outflow rate divided by SFR; their *cw* simulations), which were intended to represent supernova-driven winds, result in a MZR that fails to qualitatively match observations. The *cw* simulations produce a MZR that is flat with a very large scatter at low mass, yet becomes steep above the blowout mass, which is the critical scale above which all metals are retained. Instead, they find that their simulations with momentum-driven winds (Murray et al. 2005; Zhang & Thompson 2012) best reproduce the slope, shape, scatter, and evolution of the MZR because the wind velocity scales with the escape velocity of the halo. Their model naturally produces a FMR that shows little evolution since $z = 3$, consistent with observations (Mannucci et al. 2010; Richard et al. 2011; Cresci et al. 2012). However, their FMR does not quite reach the low observed scatter reported by Mannucci et al. (2010). Additionally, they find that the coefficient relating $M_\star$ and SFR that minimizes the scatter in the FMR is different from the one found by Mannucci et al. (2010). While there is hardly a consensus amongst galaxy evolution models about how to produce the MZR and $M_\star$–Z–SFR relation, it is clear that additional observational constraints would improve the situation. So far, the overall normalization of the MZR and the $M_\star$–Z–SFR relation have been mostly ignored by galaxy evolution models due to uncertainties in the nucleosynthetic yields used by the models and the large (up to a factor of five) uncertainties in the normalization of the observed relations caused by systematic offsets amongst metallicity calibrations. If these uncertainties could be reduced, then the normalization could be used as an additional constraint on galaxy evolution models.

The current metallicity and the metal enrichment history also have implications for certain types of stellar explosions. There is mounting evidence that long duration gamma ray bursts (Stanek et al. 2006), over-luminous type II supernovae (Stoll et al. 2011), and super-Chandrasekhar type Ia supernovae (Khan et al. 2011) preferentially occur in low metallicity environments. The progenitors of long gamma ray bursts and over-luminous type II supernovae are thought to be massive stars and the nature of their explosive death could plausibly depend on their metallicity. The cause of the association between super-Chandrasekhar type Ia supernovae and low metallicity environments is still highly uncertain because the progenitors are not well known. Nevertheless, accurate absolute metallicities for the host galaxies of the progenitors of gamma ray bursts, over-luminous supernovae, and super-Chandrasekhar type Ia supernovae will help inform the models of stellar evolution and explosions that attempt to explain these phenomena.

The uncertainty in the absolute metallicity scale can be traced to differences between the two main methods of measuring metallicity: the direct method and strong line method. The direct method utilizes the flux ratio of auroral to strong lines to measure the electron temperature of the gas, which is a good proxy for metallicity because metals are the primary coolants of H II regions. This flux ratio is sensitive to temperature because the auroral and strong lines originate from the second and first excited states, respectively, and the relative level populations depend heavily on electron temperature. The electron temperature is a strong function of metallicity, such that hotter electron temperatures correspond to lower metallicities. In the direct method, the electron temperature estimate is the critical step because the uncertainty in metallicity is nearly always dominated by the uncertainty in the electron temperature. The strong line method uses the flux ratios of the strong lines, which do not directly measure the metallicity of the H II regions but are metallicity-sensitive and can be calibrated to give approximate metallicities. The direct method is chosen over strong line methods when the auroral lines can be detected, but these lines are often too weak to detect at high metallicity. The strong lines, on the other hand, are much more easily detected than the auroral lines, particularly in metal-rich objects. Consequently, the strong line method can be used across a wide range of metallicity and on much lower signal-to-noise ratio (SNR) data, so nearly all metallicity studies of large galaxy samples employ the strong line method. Despite the convenience of the strong line method, the relationship between strong line ratios and metallicity is complicated due to the sensitivity of the strong lines to the hardness of the incident stellar radiation field and the excitation and ionization states of the gas. Thus, strong line ratios must be calibrated (1) empirically with direct method metallicities, (2) theoretically with photoionization models, or (3) semi-empirically with a combination of direct method metallicities and theoretically calibrated metallicities. Unfortunately, the three classes of calibrations do not generically produce consistent metallicities. For example, metallicities determined with theoretical strong line calibrations are systematically higher than those from the direct method or empirical strong line calibrations by up to ~ 0.7 dex (for a detailed discussion see Moustakas et al. 2010; Stasińska 2010). The various strong line methods also exhibit systematic disagreements as a function of metallicity and perform better or poorer in certain metallicity ranges.

The cause of the discrepancy between direct method metallicities and theoretically calibrated metallicities is currently unknown. As recognized by Peimbert (1967), the electron temperatures determined in the direct method might be overestimated in the presence of temperature gradients and/or fluctuations in H II regions. Such an effect would cause the direct method metallicities to be biased low (Stasińska 2005; Bresolin 2008). A similar result could arise if the traditionally adopted electron energy distribution is different from the true distribution, as suggested by Nicholls et al. (2012). Alternatively, the photoionization models that serve as the basis for the theoretical strong line calibrations, such as CLOUDY (Fer-

land et al. 1998) and MAPPINGS (Sutherland & Dopita 1993), make simplifying assumptions in their treatment of H II regions that may result in overestimated metallicities, such as the geometry of the nebula or the age of the ionizing stars (see Moustakas et al. 2010, for a thorough discussion of these issues); however, no one particular assumption has been conclusively identified to be the root cause of the metallicity discrepancy.

In this work, we address the uncertainty in the absolute metallicity scale by using the direct method on a large sample of galaxies that span a wide range of metallicity. The uniform application of the direct method also provides more consistent metallicity estimates over a broad range in stellar mass. While the auroral lines used in the direct method are undetected in most galaxies, we have stacked the spectra of many galaxies (typically hundreds to thousands) to significantly enhance the SNR of these lines. In Section 2, we describe the sample selection, stacking procedure, and stellar continuum subtraction. Section 3 describes the direct method and strong line metallicity calibrations that we use. In Section 4, we demonstrate that mean galaxy properties can be recovered from stacked spectra. We show the electron temperature relations for the stacks in Section 3.1 and argue that T_e[O II] is a better tracer of oxygen abundance than T_e[O III] in Section 3.2. Section 5 shows the main results of this study: the MZR and $M_\star$–Z–SFR relation with the direct method. In Section 6, we present the direct method N/O relative abundance as a function of O/H and stellar mass. Section 7 details the major uncertainties in metallicity measurements and the implications for the physical processes that govern the MZR and $M_\star$–Z–SFR relation. Finally, we present a summary of our results in Section 8. For the purpose of discussing metallicities relative to the solar value, we adopt the solar oxygen abundance of $12 + \log(\text{O/H}) = 8.86$ from Delahaye & Pinsonneault (2006). Throughout this work, stellar masses and SFRs are in units of $M_\odot$ and $M_\odot$ yr^{-1}, respectively. We assume a standard ΛCDM cosmology with $\Omega_m = 0.3$, $\Omega_\Lambda = 0.7$, and $H_0 = 70$ km s^{-1} Mpc^{-1}.

2. METHOD

2.1. *Sample Selection*

The observations for our galaxy sample come from the SDSS Data Release 7 (DR7; Abazajian et al. 2009), a survey that includes $\sim$930,000 galaxies (Strauss et al. 2002) in an area of 8423 square degrees. The parent sample for this study comes from the MPA-JHU catalog[2] of 818,333 unique galaxies which have derived stellar masses (Kauffmann et al. 2003a), SFRs (Brinchmann et al. 2004), and metallicities (T04). We chose only galaxies with reliable redshifts ($\sigma_z < 0.001$) in the range $0.027 < z < 0.25$ to ensure that the [O II] $\lambda3727$ line and the [O II] $\lambda\lambda7320, 7330$ lines fall within the wavelength range of the SDSS spectrograph (3800–9200 Å).

We discard galaxies classified as AGN because AGN emission line ratios may produce spurious metallicity measurements. We adopt the Kauffmann et al. (2003b) criteria (their Equation 1) to differentiate between star-forming galaxies and AGN, which employs the emission line ratios that define the Baldwin, Phillips, and Terlevich (1981) (BPT) diagram:

$$\log([\text{O III}]\,\lambda5007/\text{H}\beta) >$$

$$0.61[\log([\text{N II}]\,\lambda6583/\text{H}\alpha) - 0.05]^{-1} + 1.3. \qquad (2)$$

We follow the T04 SNR thresholds for emission lines. Specifically, we restrict our sample to galaxies with Hβ, Hα, and [N II] $\lambda6583$ detected at $>5\sigma$. Further, we apply the AGN–star-forming galaxy cut (Equation 2) to galaxies with $>3\sigma$ detections of [O III] $\lambda5007$. We also select galaxies with [O III] $\lambda5007 < 3\sigma$ but $\log([\text{N II}]\,\lambda6583/\text{H}\alpha) < -0.4$ as star-forming to include high metallicity galaxies with weak [O III] $\lambda5007$.

At the lowest stellar masses ($\log[M_\star] < 8.6$), this initial sample is significantly contaminated by spurious galaxies, which are actually the outskirts of more massive galaxies and were targeted due to poor photometric deblending. We remove galaxies whose photometric flags include DEBLEND_NOPEAK or DEBLENDED_AT_EDGE. We also visually inspected all galaxies with $\log(M_\star) < 8.6$ and discarded any that suffered from obvious errors in the stellar mass determination (again, likely as a result of off-center targeting of a much more massive galaxy).

After all of our cuts, the total number of galaxies in our sample is 208,529 and the median redshift is $z = 0.078$. At this redshift, the 3" diameter SDSS aperture will capture light from the inner 2.21 kpc of a galaxy. Since the central regions of galaxies will tend to be more metal-rich (Searle 1971), the metallicities measured from these observations will likely be biased high due to the aperture size relative to angular extent of the galaxies. However, we expect this bias is small for most galaxies (for a more detailed discussion see Tremonti et al. 2004; Kewley et al. 2005). In particular, the galaxies with very low stellar masses and metallicities that define the low mass end of the MZR tend to be compact and have homogeneous metallicities (e.g., Kobulnicky & Skillman 1997), although many of these are excluded by the criteria proposed by Kewley et al. (2005).

2.2. *Stacking Procedure*

The primary motivation for this investigation is to measure the metallicity of galaxies with the direct method. The main challenge is that the weak [O III] $\lambda4363$ and [O II] $\lambda\lambda7320, 7330$ auroral lines are undetected in most of the individual spectra. To improve the SNR of the spectra, we stacked galaxies that are expected to have similar metallicities and hence line ratios. Given the tightness of the MZR and $M_\star$–Z–SFR relation, it is reasonable to expect that galaxies at a given stellar mass, or simultaneously a given stellar mass and SFR, will have approximately the same metallicity. Thus, we have created two sets of galaxy stacks: (1) galaxies binned in 0.1 dex in $M_\star$ from $\log(M_\star/M_\odot) = 7.0$ to 11.0 (hereafter $M_\star$ stacks) and (2) galaxies binned in 0.1 dex in $M_\star$ from $\log(M_\star/M_\odot) = 7.0$ to 11.0 *and* 0.5 dex in SFR from $\log(\text{SFR}/[M_\odot \text{ yr}^{-1}]) = -2.0$ to 2.0 (hereafter $M_\star$–SFR stacks)[3]. For convenience, we will refer to the stacks by the type of stack with a subscript and a superscript to denote the upper and lower bounds of $\log(M_\star)$ or $\log(\text{SFR})$ (e.g., $M_{\star\,8.7}^{8.8}$ is the $M_\star$ stack with $\log[M_\star/M_\odot] = 8.7$–8.8, and $\text{SFR}_{0.0}^{0.5}$ corresponds to the $M_\star$–SFR stacks with $\log[\text{SFR}/M_\odot \text{ yr}^{-1}] = 0.0$–0.5). Figure 1 shows the number of galaxies in each $M_\star$–SFR stack (each box represents a stack) with a measured metallicity (indicated by the color coding).
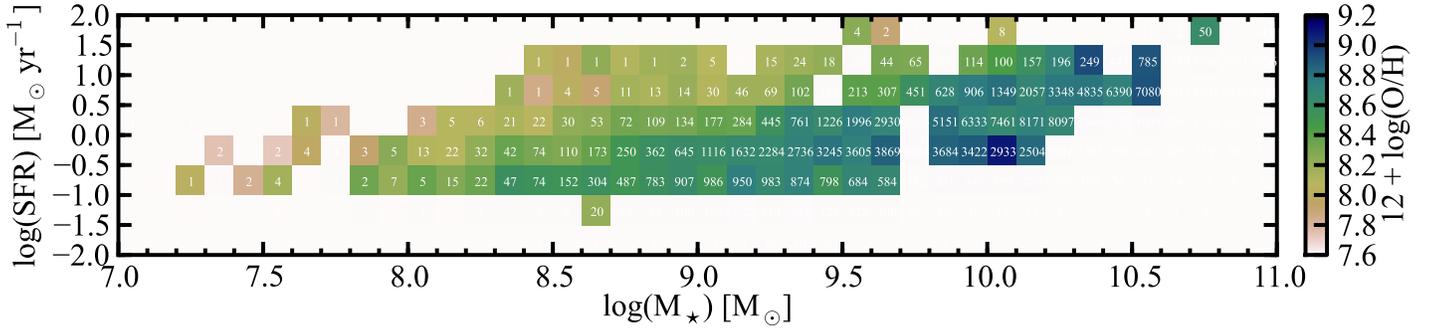
Figure 1. Number of galaxies and direct method metallicity as a function of $M_\star$ and SFR. The squares represent each $M_\star$–SFR stack, the number of galaxies is indicated by the white text, and the color scale corresponds to the metallicity. For reference, the Tremonti et al. (2004) MZR covers $\log(M_\star)$ = 8.5–11.5, and the Mannucci et al. (2010) FMR spans $\log(M_\star)$ = 9.1–11.35 and $\log(\mathrm{SFR})$ = −1.45→0.80.
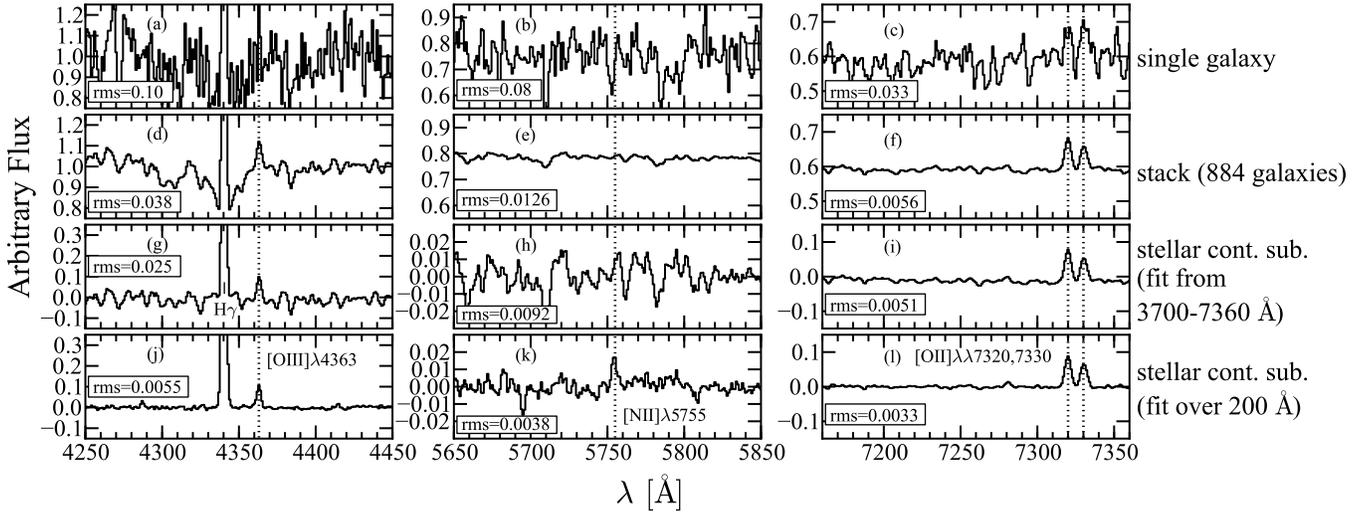
Figure 2. Sample spectra from the $\log(M_\star)$ = 8.7–8.8 (N_{gal} = 884) stack. From left to right, the three columns show the [O III] $\lambda4363$, [N II] $\lambda5755$, and [O II] $\lambda\lambda7320, 7330$ auroral lines. From top to bottom, the four rows correspond to the reduced spectrum of a single galaxy, the spectrum of the stack, the spectrum of the stack after the removal of the stellar continuum (fit from 3700–7360 Å), and the spectrum of the stack after the removal of the stellar continuum (fit to a 200 Å window near the emission line of interest). The continuum rms of each spectrum near the relevant emission line is given in the inset of each panel.

We stacked galaxy spectra that have been processed with the SDSS reduction pipeline (Stoughton et al. 2002). First, we corrected for Milky Way reddening with the extinction values from Schlegel et al. (1998). Then, the individual galaxy spectra were shifted to the rest frame with the redshifts from the MPA/JHU catalog. Next, we linearly interpolated the spectra onto a universal grid (3700–7360 Å; $\Delta\lambda$ = 1 Å) and normalized them to the mean flux from 4400–4450 Å. Finally, the spectra were co-added (i.e., we took the mean flux in each wavelength bin) to form the stacked spectra (see Section 4 for comparisons between the electron temperatures and metallicities of stacks and individual galaxies).

Figure 2 shows the SNR increase of the [O III] $\lambda4363$ (left column), [N II] $\lambda5755$ (middle column), and [O II] $\lambda\lambda7320, 7330$ (right column) lines as the spectra are processed from a typical single galaxy spectrum (top row) to the stacked spectrum (second row) to the stellar continuum subtracted spectrum (third row; see Section 2.3) or the narrow wavelength window stellar continuum subtracted spectrum (bottom row; see Section 2.3). The spectra in the top row are from a typical galaxy in the $\log(M_\star)$ = 8.7–8.8 bin; the bottom three rows show the stacked spectra from the same

bin. In each panel, we report the continuum root mean square (rms). The decrease in the continuum noise when comparing the spectra in the top row to the second row of Figure 2 is dramatic. Further significant noise reduction can be achieved by removing the stellar continuum (shown in the bottom two rows of Figure 2), as we describe in Section 2.3.

2.3. *Stellar Continuum Subtraction*

Stacking the spectra increases the SNR, but it is important to fit and subtract the stellar continuum to detect and accurately measure the flux of these lines, especially [O III] $\lambda4363$ due to its proximity to the Hγ stellar absorption feature. We subtracted the stellar continuum with synthetic template galaxy spectra created with the STARLIGHT stellar synthesis code (Cid Fernandes et al. 2005), adopted the Cardelli et al. (1989) extinction law, and masked out the locations of the emission lines. The synthetic spectra were created from a library of 300 empirical MILES spectral templates (Sánchez-Blázquez et al. 2006; Vazdekis et al. 2010, data as obtained from the MILES website[4]). The MILES templates provided an

[4] http://miles.iac.es/

Table 1
Wavelength Fit and Mask Ranges of
Measured Lines

Line	Fit Range [Å]	Mask Range [Å]
(1)	(2)	(3)
[O II] λ3727	3700–4300	3710–3744
[Ne III] λ3868	3800–4100	3863–3873
[S II] λ4069	3950–4150	$\cdots$
Hγ λ4340	4250–4450	4336–4344
[O III] λ4363	4250–4450	4360–4366
He II λ4686	4600–4800	4680–4692
[Ar IV] λ4740	3700–4700	$\cdots$
Hβ λ4861	3700–7360	4857–4870
[O III] λ4959	3700–7360	4954–4964
[O III] λ5007	3700–7360	5001–5013
[N II] λ5755	5650–5850	5753–5757
[S III] λ6312	6100–6500	6265–6322
[N II] λ6548	3700–7360	6528–6608
Hα λ6563	3700–7360	6528–6608
[N II] λ6583	3700–7360	6528–6608
[S II] λ6716	3700–7360	6696–6752
[S II] λ6731	3700–7360	6696–6752
[Ar III] λ7135	7035–7235	7130–7140
[O II] λ7320	7160–7360	7318–7322
[O II] λ7330	7160–7360	7328–7332

Note. — Column (1): Emission lines.
Column (2): The wavelength range of the
stellar continuum fit. Column (3) The
wavelength range of the stellar contin-
uum fit that was masked out.

Table 2
Line Fluxes

Column	Format	Description
1	F4.1	Lower stellar mass limit of the stack
2	F4.1	Upper stellar mass limit of the stack
3	F4.1	Lower SFR limit of the stack
4	F4.1	Upper SFR limit of the stack
5	I5	Number of galaxies in the stack
6	F6.2	[O II] λ3727 line flux
7	F5.2	Error on [O II] λ3727 line flux
8	F5.2	[Ne III] λ3868 line flux
9	F4.2	Error on [Ne III] λ3868 line flux
10	F4.2	[S II] λ4069 line flux
11	F4.2	Error on [S II] λ4069 line flux
12	F6.2	Hγ line flux
13	F5.2	Error on Hγ line flux
14	F5.2	[O III] λ4363 line flux
15	F4.2	Error on [O III] λ4363 line flux
16	F4.2	He II λ4686 line flux
17	F4.2	Error on He II λ4686 line flux
18	F4.2	[Ar IV] λ4740 line flux
19	F4.2	Error on [Ar IV] λ4740 line flux
20	F6.2	[O III] λ4959 line flux
21	F4.2	Error on [O III] λ4959 line flux
22	F6.2	[O III] λ5007 line flux
23	F5.2	Error on [O III] λ5007 line flux
24	F4.2	[N II] λ5755 line flux
25	F4.2	Error on [N II] λ5755 line flux
26	F4.2	[S III] λ6312 line flux
27	F4.2	Error on [S III] λ6312 line flux
28	F5.2	[N II] λ6548 line flux
29	F4.2	Error on [N II] λ6548 line flux
30	F6.2	Hα line flux
31	F5.2	Error on Hα line flux
32	F6.2	[N II] λ6583 line flux
33	F4.2	Error on [N II] λ6583 line flux
34	F6.2	[S II] λ6716 line flux
35	F4.2	Error on [S II] λ6716 line flux
36	F5.2	[S II] λ6731 line flux
37	F4.2	Error on [S II] λ6731 line flux
38	F4.2	[Ar III] λ7135 line flux
39	F4.2	Error on [Ar III] λ7135 line flux
40	F4.2	[O II] λ7320 line flux
41	F4.2	Error on [O II] λ7320 line flux
42	F4.2	[O II] λ7330 line flux
43	F4.2	Error on [O II] λ7330 line flux

Note. — This table is published in its entirety in the
electronic edition of the journal. The column names
are shown here for guidance regarding its form and
content.

excellent fit to the stellar continuum (see bottom two rows of
Figure 2). We note the MILES templates yielded better fits to
the very high SNR spectra than the Bruzual & Charlot (2003)
spectral templates, based on the STELIB (Le Borgne et al.
2003) library, likely due to the higher resolution (0.9 Å) of
the MILES templates compared to the STELIB (3.0 Å).

We performed stellar template fits to the entire spectral
range, select subregions centered on weak lines of interest,
and subregions around the strong lines blueward of 4000 Å.
The latter are situated amongst a forest of stellar absorption
lines. The line fluxes of the strong emission lines redward of
4000 Å (Hβ, [O III] $\lambda\lambda$4959, 5007, Hα, [N II] $\lambda\lambda$6548, 6583,
and [S II] $\lambda\lambda$6716, 6731) were measured from the spectrum
where the stellar continuum was fit over the full wavelength
range of our stacked spectra (λ = 3600–7360 Å; see third row
of Figure 2). The stellar continuum subtraction near weak
emission lines ([S II] λ4069, [O III] λ4363, He II λ4686,
[N II] λ5755, [S III] λ6312, [Ar IV] λ4740, and [O II]
$\lambda\lambda$7320, 7330) and blue strong emission lines ([O II] λ3727
and [Ne III] λ3868) was improved if the stellar continuum
fit was restricted to limited wavelength ranges within a few
100 Å of the line of interest (compare the third and bottom
rows of Figure 2). For the weak lines and blue strong lines, we
measured the line fluxes from the stellar continuum subtracted
spectra within these narrow wavelength windows (details are
listed in Table 1). In order to compare the line fluxes across re-
gions with different stellar continuum subtraction (e.g., from
portions of the spectrum that were fit with smaller wavelength
ranges), we denormalized the spectra after the STARLIGHT fit.

2.4. *Automated Line Flux Measurements*

We used the *specfit* task (Kriss 1994) in the IRAF/STSDAS
package to automatically fit emission lines with a χ^2 mini-

mization algorithm. We simultaneously fit a flat continuum
and Gaussian line profiles for the emission lines, even if
lines were blended. For doublets, we fixed the width of the
weaker line by pinning its velocity width to the stronger line
([O II] λ3726 to [O II] λ3729, [O III] λ4959 to [O III] λ5007,
[N II] λ6548 to [N II] λ6583, [S II] λ6731 to [S II] λ6716,
and [O II] λ7330 to [O II] λ7320). We also included the
continuum rms of the spectrum as an input to the fitting pro-
cedure. After experimenting with several different χ^2 min-
imization algorithms implemented within *specfit*, we chose
the simplex algorithm because of its consistent convergence,
particularly for weak lines. Line fluxes measured by *specfit*
generally agreed well with line fluxes measured interactively
with the OSU LINER package. The uncertainty in the line flux
is based on the χ^2 fit returned from *specfit*. Finally, all line
fluxes were corrected for reddening with the extinction law
from Cardelli et al. (1989) and the assumption that the intrin-
sic ratio of the Balmer lines is set by case B recombination
(F[Hα]/F[Hβ] = 2.86 for T_e = 10,000 K). The line fluxes are

presented in an online table whose columns are described in Table 2.

We disregarded lines that were poorly fit (negative flux, uncertainty in central wavelength >1 Å, had uncertainty in the velocity width of >100 km/s, or had low SNR [<5σ]). Further care was taken to ensure the robustness of [O III] $\lambda4363$ flux measurements. As $M_\star$ increased to moderate values ($\log[M_\star] > 9.0$), an unidentified emission feature at 4359 Å became blended with the [O III] $\lambda4363$ line, which limited the SNR of the line flux measurement independent of the continuum rms. We are unsure of the origin of this feature, but it could be caused by an over-subtraction in the stellar continuum fit. We simultaneously fit the 4359 Å feature and [O III] $\lambda4363$ and pinned the velocity width of both lines to Hγ. If F(4359) > 0.5 F(4363), then we determined that [O III] $\lambda4363$ could not be robustly fit. If [O III] $\lambda4363$ could be well fit, we refit it with a single Gaussian whose velocity width was pinned to Hγ. The line flux measurements from the single Gaussian fitting agreed better with interactive line flux measurements than the deblended line flux measurements. The remaining weak lines are in regions without strong stellar absorption features. Often, the [O II] $\lambda\lambda7320, 7330$ lines could be detected in the stacked spectra without the stellar continuum fit (see Figure 2f). The [N II] $\lambda5755$ and [S II] $\lambda4069$ auroral lines were usually too weak to be detected without stellar continuum subtraction.

Optical recombination lines, such as C II $\lambda4267$ and O II $\lambda4649$, are also sensitive to metallicity. Unlike auroral lines, they are almost independent of temperature, so they could provide a useful check on the direct method metallicities. Unfortunately, optical recombination lines tend to be very weak (e.g., the median O II $\lambda4649$/[O III] $\lambda4363$ ratio of five extragalactic H II regions studied by Esteban et al. 2009 was 0.08), and we did not detect them in the stacked spectra.

3. ELECTRON TEMPERATURE AND DIRECT ABUNDANCE DETERMINATION

3.1. *Electron Temperatures*

Different ionic species probe the temperature of different ionization zones of H II regions (e.g., Stasińska 1982; Garnett 1992). In the two-zone model, the high ionization zone is traced by [O III], and the low ionization zone is traced by [O II], [N II], and [S II]. Campbell et al. (1986) used the photoionization models of Stasińska (1982) to derive a linear relation between the temperatures in these zones,

$$T_e[\text{O II}] = T_e[\text{N II}] = T_e[\text{S II}] = 0.7 T_e[\text{O III}] + 3000, \quad (3)$$

where T_e is in units of K. Subsequently, we will refer to this relation as the T_2–T_3 relation (see Pagel et al. 1992 and Izotov et al. 2006 for alternative formulations of the T_2–T_3 relation). This relation is especially useful to infer the abundance of unseen ionization states, a critical step in measuring the total oxygen abundance. While convenient, this theoretical relation may be one of the biggest uncertainties in the direct method because it is not definitively constrained by observations due to the large random errors in the flux of [O II] $\lambda\lambda7320, 7330$ (e.g., see Kennicutt et al. 2003; Pilyugin et al. 2006). The high SNR of our stacked spectra enables us to measure the electron temperature of both the high and low ionization zones for many of our stacks.

We measured the electron temperature of [O III], [O II], [N II], and [S II] with the *nebular.temden* routine (Shaw & Dufour 1995) in IRAF/STSDAS, which is based on the five level atom program of De Robertis et al. (1987). This routine determines the electron temperature from the flux ratio of the auroral to strong emission line(s) for an assumed electron density. The diversity of these temperature diagnostics are valuable cross-checks and provide an independent check on the applicability of the T_2–T_3 relation; however, for measuring oxygen abundances, we only use T_e[O III] and T_e[O II]. The electron density (n_e) can be measured from the density sensitive [S II] $\lambda\lambda6716, 6731$ doublet (cf., Cai & Pradhan 1993). For 6/45 of the $M_\star$ stacks and 65/228 of the $M_\star$–SFR stacks, the F([S II] $\lambda6716$) / F([S II] $\lambda6731$) was above the theoretical maximum ratio of 1.43 (Osterbrock 1989), which firmly places these galaxies in the low density regime, and we assume $n_e = 100$ cm^{-3} for our analysis. Yin et al. (2007) found similar inconsistencies between the theoretical maximum and measured flux ratios for individual galaxies, which suggests that there might be a real discrepancy between the maximum observed and theoretical values of F([S II] $\lambda6716$) / F([S II] $\lambda6731$).

We calculated the electron temperature and density uncertainties by propagating the line flux uncertainties with Monte Carlo simulations. For the simulations, we generated 1,000 realizations of the line fluxes (Gaussian distributed according to the 1σ uncertainty) and processed these realizations through *nebular.temden*. The electron temperatures of the stacks are given in Table 3 (full version available online).

In Figure 3, we plot the electron temperatures of [O II], [N II], and [S II] against the [O III] electron temperature for the $M_\star$ stacks (left column; open circles) and the $M_\star$–SFR stacks (right column; circles color-coded by SFR). For comparison, we show the T_2–T_3 relation (Equation 3) as the black line in each panel. In all three T_e–T_e plots, the $M_\star$ stacks form a tight locus that falls within the distribution of $M_\star$–SFR stacks. The $M_\star$–SFR stacks show a large dispersion in T_e[O II] at fixed T_e[O III] that is not present in the $M_\star$ stacks. Most of this scatter is due to stacks with SFR$_{1.0}^{1.5}$, which approach and exceed the T_e[O II]–T_e[O III] relation. On the other hand, the $M_\star$–SFR stacks show little scatter in the T_e[N II]–T_e[O III] and T_e[S II]–T_e[O III] plots, and they track the $M_\star$ stacks in these plots.

The vast majority of the stacks in Figure 3 fall below the T_2–T_3 relation, independent of the type of stacks ($M_\star$ or $M_\star$–SFR) or the tracer ion ([O II], [N II], or [S II]). The multiple temperature indicators show that the T_2–T_3 relation overpredicts the temperature in the low ionization zone (or underpredicts the temperature in the high ionization zone). If we assume that T_e[O III] is accurate (i.e., the temperature in the low ionization zone is overestimated by the T_2–T_3 relation), then the median offsets from the T_2–T_3 relation for the $M_\star$ stacks and the $M_\star$–SFR stacks, respectively, are

- T_e[O II]: −2000 K and −1300 K,

- T_e[N II]: −1200 K and −1400 K,

- T_e[S II]: −4100 K and −3300 K.

The T_e[O II] and T_e[N II] offsets from the T_2–T_3 relation for the $M_\star$ stacks are consistent given the scatter, which suggests that the T_2–T_3 relation overestimates the low ionization zone T_e by ∼1000–2000 K. The T_e[S II] measurements show a larger offset from the T_2–T_3 relation than T_e[O II] and T_e[N II]. The outlier in the $M_\star$–SFR T_e[S II]–T_e[O III] panel also has a high T_e[O II], but this outlier just corresponds to a single galaxy,

Table 3
Electron Temperatures, Metallicity, and N/O Abundance

log($M_\star$) [M$_\odot$]		log(SFR) [M$_\odot$ yr^{-1}]		$N_{\rm gal}$	$T_{\rm e}$[O III] [K]	$T_{\rm e}$[O II] [K]	$T_{\rm e}$[N II] [K]	$T_{\rm e}$[S II] [K]	12 + log(O/H) [dex]	log(N/O) [dex]
(1)	(2)	(3)	(4)	(5)	(6)	(7)	(8)	(9)	(10)	(11)
					$M_\star$ Stacks					
7.0	7.1			1	⋯	⋯	⋯	⋯	⋯	⋯
7.1	7.2			4	⋯	⋯	⋯	⋯	⋯	⋯
7.2	7.3			4	14000 ± 600	⋯	⋯	⋯	⋯	⋯
7.3	7.4			4	17500 ± 200	⋯	⋯	⋯	⋯	⋯
7.4	7.5			2	15700 ± 200	12800 ± 800	⋯	⋯	7.82 ± 0.03	⋯
⋮	⋮	⋮	⋮	⋮	⋮	⋮	⋮	⋮	⋮	⋮
					$M_\star$–SFR Stacks					
7.0	7.1	0.0	0.5	1	⋯	⋯	⋯	⋯	⋯	⋯
7.1	7.2	-0.5	0.0	1	⋯	⋯	⋯	⋯	⋯	⋯
7.1	7.2	0.0	0.5	2	⋯	⋯	⋯	⋯	⋯	⋯
7.2	7.3	-1.0	-0.5	1	13400 ± 500	11800 ± 700	⋯	⋯	8.04 ± 0.04	⋯
7.2	7.3	-0.5	0.0	2	⋯	⋯	⋯	⋯	⋯	⋯
⋮	⋮	⋮	⋮	⋮	⋮	⋮	⋮	⋮	⋮	⋮

Note. — Column (1): Lower stellar mass limit of the stack. Column (2): Upper stellar mass limit of the stack. Column (3): Lower SFR limit of the stack. Column (4): Upper SFR limit of the stack. Column (5): Number of galaxies in the stack. Columns (6)–(9): Electron temperatures for [O III], [O II], [N II], and [S II]. Column (10): Direct method metallicity. Column (11): N/O abundance.

(This table is published in its entirety in the electronic edition of the journal. A portion is shown here for guidance regarding its form and content.)

so it may not be representative of all galaxies with this stellar mass and SFR.

The offset between the electron temperatures of the stacks and the T_2–T_3 relation is analogous to the trend for individual galaxies found by Pilyugin et al. (2010), which persists when these galaxies are stacked (see Section 4 and Figure 8a). The similar distributions of stacks and individual galaxies relative to the T_2–T_3 relation shows that the offset for the stacks is not a by-product of stacking but rather a reflection of the properties of the individual galaxies.

At high SFRs (SFR$^{1.5}_{1.0}$ and SFR$^{2.0}_{1.5}$), the offset in $T_{\rm e}$[O II] disappears, and the median $T_{\rm e}$[O II] of these stacks is consistent with the T_2–T_3 relation, albeit with a large dispersion. The emission from these galaxies is likely dominated by young stellar populations, whose hard ionizing spectrum may be similar to the single stellar spectra used by Stasińska (1982) to model H II regions. However, a single stellar effective temperature may not be appropriate for galaxy spectra that include a substantial flux contribution from older H II regions that have softer ionizing spectra (Kennicutt et al. 2000; Pilyugin et al. 2010).

Figure 4 compares the electron temperatures of [O II] and [N II] for the $M_\star$–SFR stacks (color-coded by SFR). In the two-zone model, both $T_{\rm e}$[O II] and $T_{\rm e}$[N II] represent the temperature of the low ionization zone, so these temperatures should be the same. The stacks scatter around the line of equality (black line), though the median offset from the $T_{\rm e}$[O II] = $T_{\rm e}$[N II] relation is 1100 K towards higher $T_{\rm e}$[N II]. If only the stacks that also have detectable [O III] $\lambda4363$ are considered (most of which have $T_{\rm e}$[O II] $\gtrsim$ 8000 K), then the median offset from the relation is smaller than the median uncertainty on $T_{\rm e}$[N II]. The agreement between $T_{\rm e}$[O II] and $T_{\rm e}$[N II] for this subset of stacks is consistent with the similar offsets found for $T_{\rm e}$[O II] and $T_{\rm e}$[N II] relative to the T_2–T_3

relation in Figure 3.

3.2. *Ionic and Total Abundances*

We calculated the ionic abundance of O$^+$ and O^{++} with the *nebular.ionic* routine (De Robertis et al. 1987; Shaw & Dufour 1995) in IRAF/STSDAS, which determines the ionic abundance from the electron temperature, electron density, and the flux ratio of the strong emission line(s) relative to Hβ. We derived the ionic abundance uncertainties with the same Monte Carlo simulations used to compute the electron temperature and density uncertainties (see Section 3.1); the ionic abundance uncertainties were propagated analytically to calculate the total abundance uncertainties. We do not attempt to correct for systematic uncertainties in the absolute abundance scale.

The top two panels of Figure 5 show the ionic abundance of O$^+$ and O^{++} as a function of stellar mass for the $M_\star$ stacks (open circles) and the $M_\star$–SFR stacks (circles color-coded by SFR). The O$^+$ abundance increases with stellar mass at fixed SFR and decreases with SFR at fixed stellar mass. The abundance of O^{++} is relatively constant as a function of stellar mass but is detected in galaxies with progressively higher SFRs as stellar mass increases.

In Figure 5c, we plot the logarithmic ratio of the O^{++} and O$^+$ abundances as a function of stellar mass. The dotted line in Figure 5c shows equal abundances of O$^+$ and O^{++}. The contribution of O$^+$ to the total oxygen abundance increases with stellar mass at fixed SFR and decreases with SFR at fixed stellar mass (i.e., in the same sense as how the O$^+$ abundance changes with $M_\star$ and SFR). The *O$^+$ abundance dominates the total oxygen abundance in the majority of the stacks* (i.e., above log[$M_\star$] = 8.2 for the $M_\star$ stacks and in half of the $M_\star$–SFR stacks with detected [O II] $\lambda\lambda7320$, 7330). Furthermore, the O$^+$ abundance can be measured in many high stellar mass
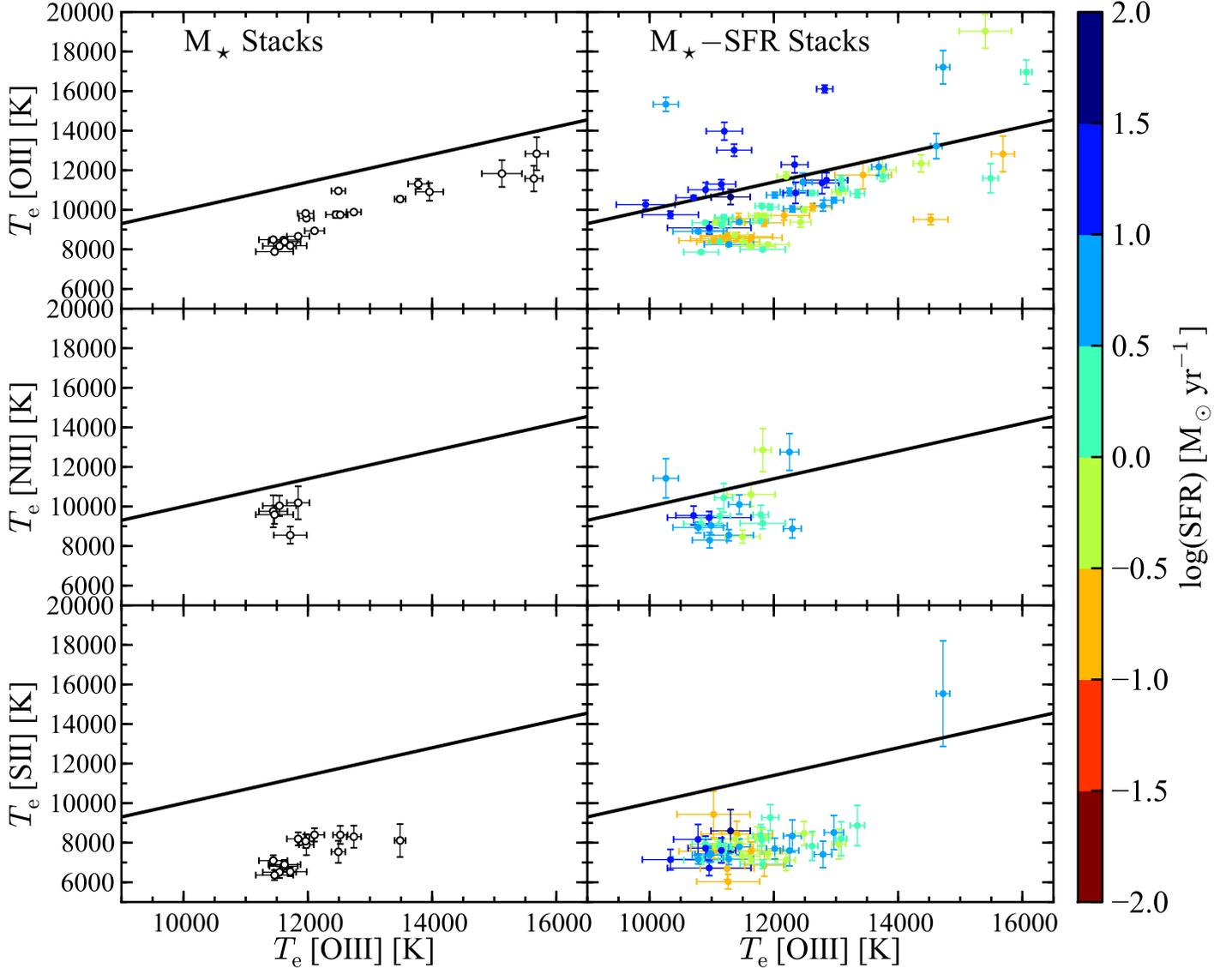
Figure 3. Electron temperatures derived from the [O II], [N II], and [S II] line ratios plotted as a function of electron temperature derived from the [O III] line ratio for the $M_\star$ stacks (left column) and $M_\star$–SFR stacks (right column; color-coded by SFR). The lines in the top, middle, and bottom rows show the T_e[O II]–T_e[O III], T_e[N II]–T_e[O III], and T_e[S II]–T_e[O III] relations (Equation 3), respectively. The outlier in the lower right panel is a single galaxy, so it may not be representative of all galaxies with this stellar mass and star formation rate.

and/or low SFR stacks that lack a measured O^{++} abundance, which indicates that O^+ is very likely the main ionic species of oxygen in these stacks too. A simple extrapolation of the $\log(O^{++}/O^+)$ ratio to higher stellar masses for the $M_\star$ stacks shows that the O^{++} abundance would contribute less than 10% of the total oxygen abundance.

We assume that the total oxygen abundance is the sum of the ionic abundances of the two dominant species,

$$\frac{O}{H} = \frac{O^+}{H^+} + \frac{O^{++}}{H^+}, \qquad (4)$$

and the total abundance uncertainties were determined by propagating the ionic abundance uncertainties. In highly ion-

ized gas, oxygen may be found as O^{3+}, but its contribution to the total oxygen abundance is minimal. Abundance studies that use the direct method typically measure T_e[O III] and the O^{++} abundance but adopt the T_2–T_3 relation to infer T_e[O II] and the O^+ abundance. However, Figure 3 shows that the T_2–T_3 relation overestimates T_e[O II], which leads to an underestimate of the O^+ abundance and the total oxygen abundance. Many of the stacks have measured O^+ and O^{++} abundances, so the total oxygen abundance can be measured accurately in these stacks without using the T_2–T_3 relation.

To extend our total oxygen abundance measurements to higher stellar mass, we form a "composite" metallicity calibration (see Figure 6) that uses the O^+ and O^{++} abundances when available and the O^+ abundance plus the O^{++} abundance
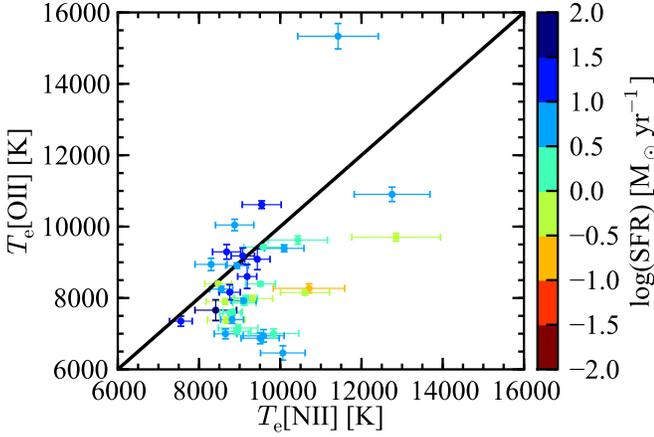
Figure 4. Electron temperatures derived from the [O II] line ratios as a function of electron temperature derived from the [N II] line ratios for the $M_\star$–SFR stacks (color-coded by SFR). The line indicates T_e[O II] = T_e[N II] (as assumed in Equation 3).
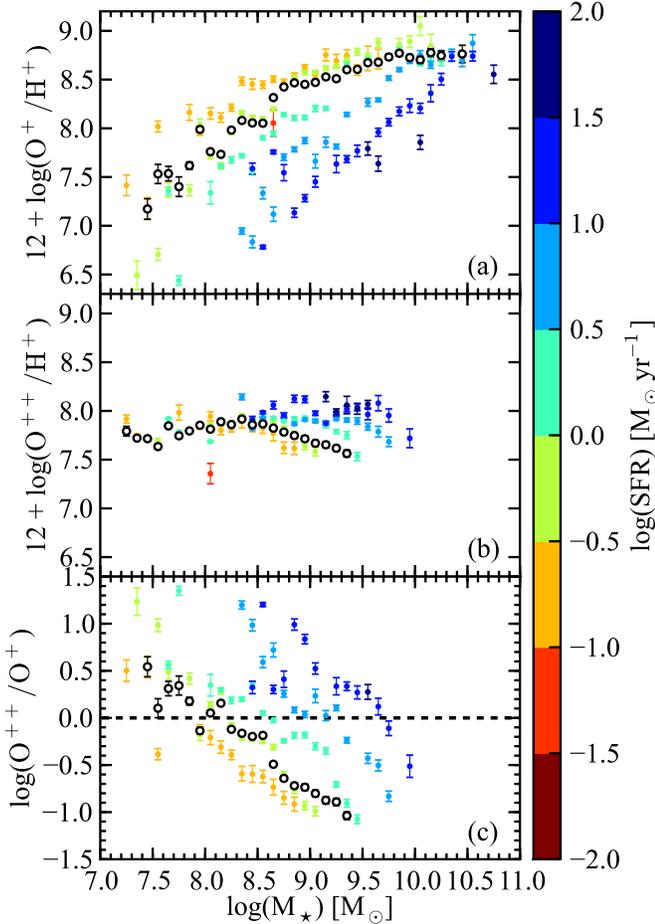
Figure 5. The ionic abundance of O^+ (panel a), the ionic abundance of O^{++} (panel b), and the relative ionic abundance of O^{++} and O^+ (panel c) as a function of stellar mass for the $M_\star$ stacks (open circles) and $M_\star$–SFR stacks (circles color-coded by SFR). The dashed line in panel c indicates equal abundances of O^{++} and O^+.
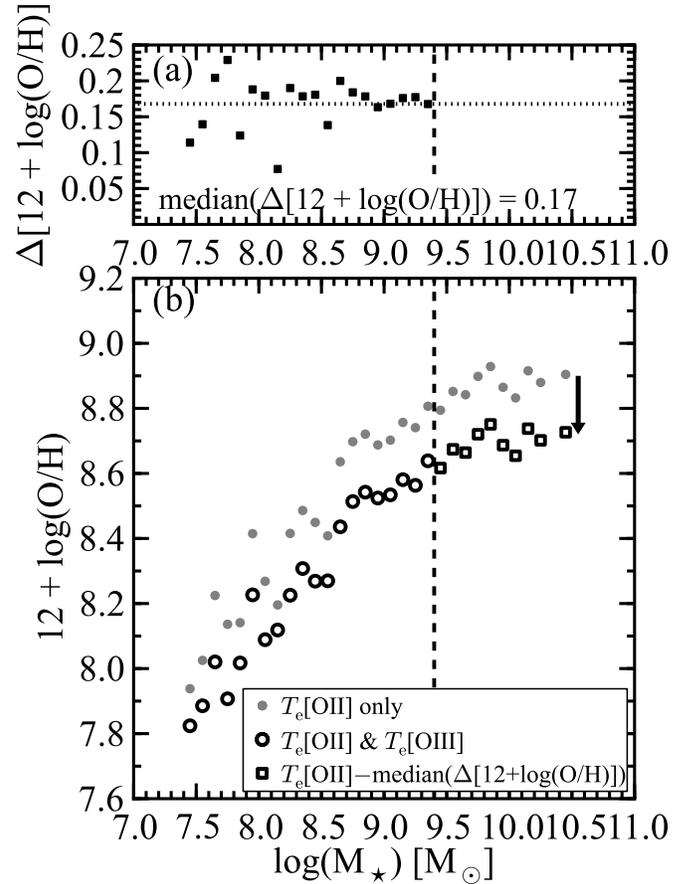
Figure 6. Panel (a): the difference in the direct method metallicity determined from T_e[O II] only (T_e[O III] was inferred with the T_2–T_3 relation given in Equation 3) and the direct method metallicity determined from both T_e[O II] and T_e[O III]. The dotted line denotes the median difference, and the dashed line marks the upper mass cutoff for which T_e[O III] can be independently measured in the $M_\star$ stacks. Panel (b): the mass-metallicity relation for direct method metallicities determined from T_e[O II] only (gray circles) and from both T_e[O II] and T_e[O III] (open circles). To account for the overestimated metallicity (and underestimated T_e[O III]) caused by assuming the T_2–T_3 relation (Equation 3), we subtract the median metallicity difference shown in panel (a) from the T_e[O II]-based metallicities above $\log(M_\star) = 9.4$ (shown by the dashed line), which results in the open squares. The arrow marks this shift. The sequence of open circles and squares shows the composite direct method metallicities of the $M_\star$ stacks that we will adopt for the rest of the paper. We repeated the same procedure for each SFR bin of the $M_\star$–SFR stacks. The median metallicity differences are given in Table 4.

inferred with the T_2–T_3 relation if T_e[O II] is measured but not T_e[O III] (in the opposite sense from how it is normally applied). The total oxygen abundance of the latter group of stacks is dominated by the O^+ abundance, so the inferred O^{++} abundance makes only a small contribution (<10% based on the trend indicated by Figure 5c). A simple combination of these two metallicity calibrations would lead to a discontinuity at their interface (in the MZR) because applying the T_2–T_3 relation underestimates T_e[O III] and thus overestimates the O^{++} abundance. To account for this effect, we decrease the total oxygen abundances that adopt the T_2–T_3 relation by the median offset between the two calibrations where they are both measured (0.18 dex for the $M_\star$ stacks). For the $M_\star$–SFR stacks, we calculate the median offset for each SFR bin (reported in Table 4). The offsets are nearly constant as a function of $M_\star$ and stem from the approximately constant offset in the T_e[O II]–T_e[O III] plot (top row of Figure 3). Because we account for the systematic offset from the T_2–T_3 relation,

our composite metallicities are insensitive to the exact choice of the T_2–T_3 relation. The metallicities of the stacks are presented in Table 3.

Most direct method metallicity studies measure the [O III] $\lambda4363$ line flux but not the [O II] $\lambda\lambda7320, 7330$ line fluxes, so they must adopt a T_e[O II]–T_e[O III] relation, such as the T_2–T_3 relation, to estimate the O^+ abundance. One reason for this is the large wavelength separation between the [O II] $\lambda3727$ strong line and the [O II] $\lambda\lambda7320, 7330$ auroral lines used to measure T_e[O II]. The flux ratio of these two line complexes can be affected by a poor reddening correction, particularly for the [O II] $\lambda3727$ line, and some spectrographs cannot observe this entire wavelength range efficiently. In individual spectra, the [O II] $\lambda\lambda7320, 7330$ lines can be overwhelmed by the noise, which can lead to a large scatter in the T_e[O II]–T_e[O III] diagram (see Figure 1 of Kennicutt et al. 2003 or Figure 4 of Izotov et al. 2006). Fortunately, the noise near [O II] $\lambda\lambda7320, 7330$ appears to be random and is effectively reduced by stacking, even without the stellar continuum subtraction (see Figure 2f). Kennicutt et al. (2003) noted that the [O II] $\lambda\lambda7320, 7330$ line fluxes may be affected by recombination of O^{++}, although they find that the typical contribution to the [O II] $\lambda\lambda7320, 7330$ line fluxes is <5% (based on the correction formulae from Liu et al. 2000) and that T_e[O II] is affected by ∼2–3%, which corresponds to <400 K for the H II regions in their study.

We also calculated the ionic abundance of N^+ with *nebular.ionic*, similar to the procedure used to calculate the ionic abundances of O^+ and O^{++}, except that we adopt T_e[O II] as the electron temperature instead of T_e[N II] because the [O II] $\lambda\lambda7320, 7330$ lines are detected in more stacks and with higher SNR than the [N II] $\lambda5755$ line (see Figure 2). The relative ionic abundance of N^+/O^+ was derived from the ionic abundances of each species. We then assume that $N/O = N^+/O^+$ (Peimbert & Costero 1969; Garnett 1990) to facilitate comparison with other studies in the literature (e.g., Vila Costas & Edmunds 1993). Although this assumption is uncertain, Nava et al. (2006) found that it should be accurate to ∼10% for low metallicity objects ($12 + \log[O/H] \leq 8.1$). The N/O abundances of the stacks are reported in Table 3.

3.3. *Strong Line Metallicities*

We compare our direct method metallicities to strong line metallicities with various empirical and theoretical calibrations of the most common line ratios:

- R_{23}: ([O II] $\lambda3727$ + [O III] $\lambda\lambda4959, 5007$) / Hβ

- N2O2: [N II] $\lambda6583$ / [O II] $\lambda3727$,

- N2: [N II] $\lambda6583$ / Hα,

- O3N2: ([O III] $\lambda5007$ / Hβ) / ([N II] $\lambda6583$ / Hα).

We derived metallicities for our stacks with the theoretical R_{23} calibrations of McGaugh (1991, hereafter M91), Zaritsky et al. (1994, hereafter Z94), and Kobulnicky & Kewley (2004, hereafter KK04); the hybrid empirical–theoretical N2 calibration of Denicoló et al. (2002, hereafter D02); the theoretical N2O2 calibration of Kewley & Dopita (2002, hereafter KD02); and the mostly empirical N2 and O3N2 calibrations of Pettini & Pagel (2004, hereafter PP04). We determined uncertainties on the strong line metallicities with the Monte Carlo simulations detailed in Section 3.1; these uncertainties do not account for systematic uncertainties in the
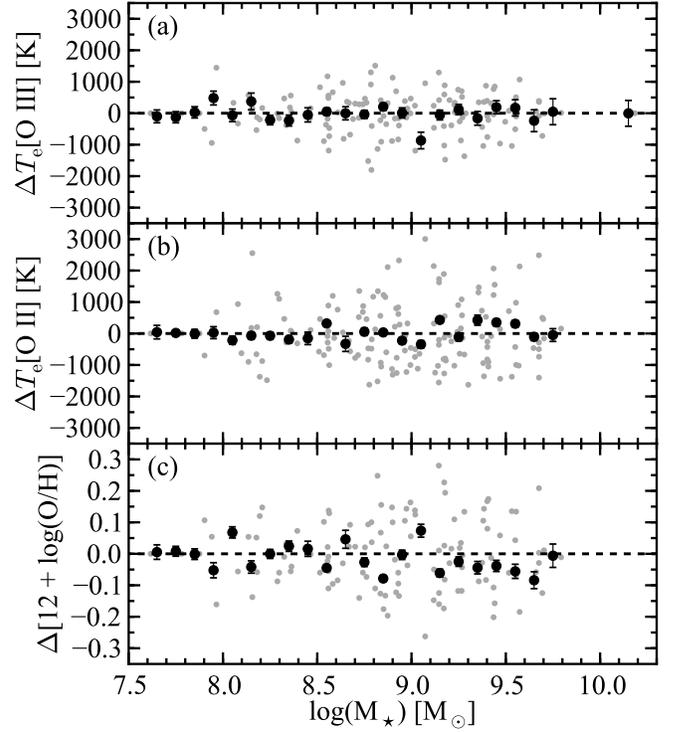

Figure 7. T_e[O III], T_e[O II], and direct method metallicity for individual spectra (small gray circles) and stacks in bins of 0.1 dex in stellar mass (large black circles) for the Pilyugin et al. (2010) sample relative to the mean of galaxies within a stellar mass bin of width 0.1 dex $M_\odot$ (shown by the dashed line in each panel). The stacks are consistent with the mean T_e[O III], T_e[O II], and metallicity within the measurement uncertainties.

absolute abundance scale. For a detailed discussion of these calibrations and formulae to convert between the metallicities derived from each calibration see Kewley & Ellison (2008).

4. HOW DOES STACKING AFFECT MEASURED ELECTRON TEMPERATURES AND METALLICITIES?

Stacking greatly increases SNR and thus enables measurements of physical properties that are unattainable for individual objects. However, measurements from stacked spectra are only meaningful if they represent the typical properties of the objects that went into the stack. To evaluate the effect of stacking on the electron temperatures and metallicities, we stacked a sample of 181 SDSS DR6 (Adelman-McCarthy et al. 2008) galaxies with individual detections of [O III] $\lambda4363$ and [O II] $\lambda\lambda7320, 7330$ from Pilyugin et al. (2010) in bins of 0.1 dex in stellar mass. Figure 7 shows the T_e[O III], T_e[O II], and the direct method metallicities of the individual galaxies (gray squares) and stacks (black circles) relative to the mean of the galaxies that went into each stack. For all three properties, the stacks are consistent with the mean of the galaxies within the measurement uncertainties, which demonstrates that the properties derived from galaxies stacked in narrow bins of stellar mass are representative of the mean properties of the input galaxies.

In Figure 8, the [O II], [N II], and [S II] electron temperatures are plotted as a function of the [O III] electron temperature for the galaxies (squares color-coded by SFR) and stacks (black circles). The black line in each panel indicates the T_2–T_3 relation (Equation 3). The stacks fall within the distribution of galaxies in the T_e[O II]–T_e[O III] and T_e[S II]–T_e[O III] plots (Figure 8a,c). There is some discrepancy between the
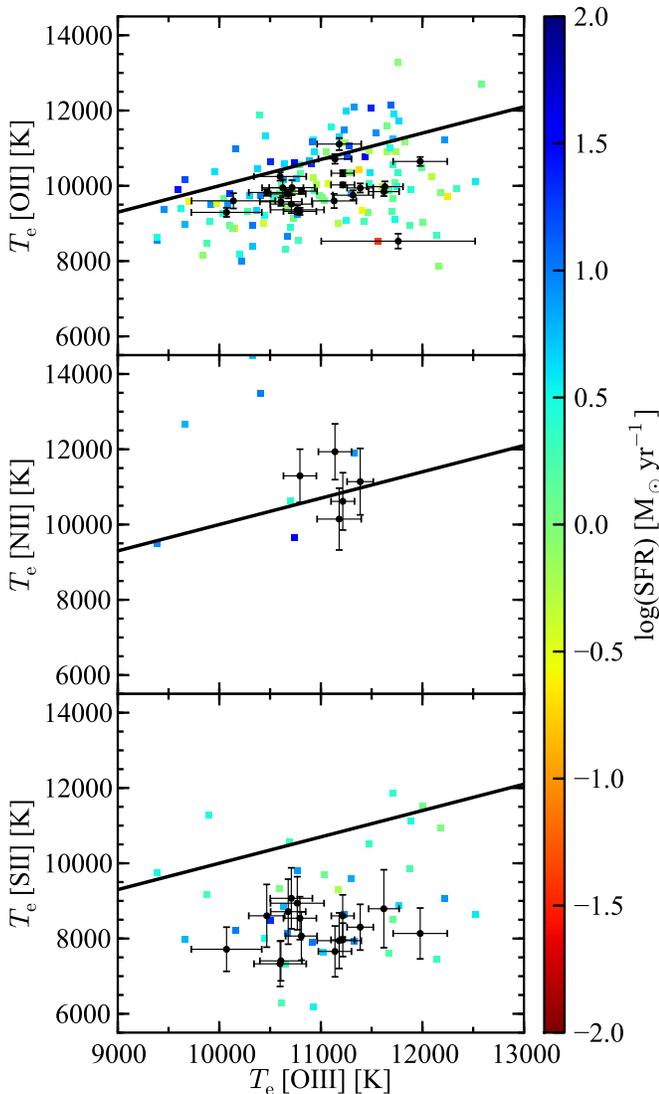
Figure 8. The electron temperatures derived from the [O II], [N II], and [S II] line ratios as a function of electron temperature derived from the [O III] line ratio for the Pilyugin et al. (2010) sample of galaxies with detectable [O III] $\lambda4363$ and [O II] $\lambda\lambda7320, 7330$ (squares color-coded by SFR; see Section 4) and stacks of the same galaxies in bins of 0.1 dex in stellar mass (black circles). The black line shows the T_2–T_3 relation (Equation 3).
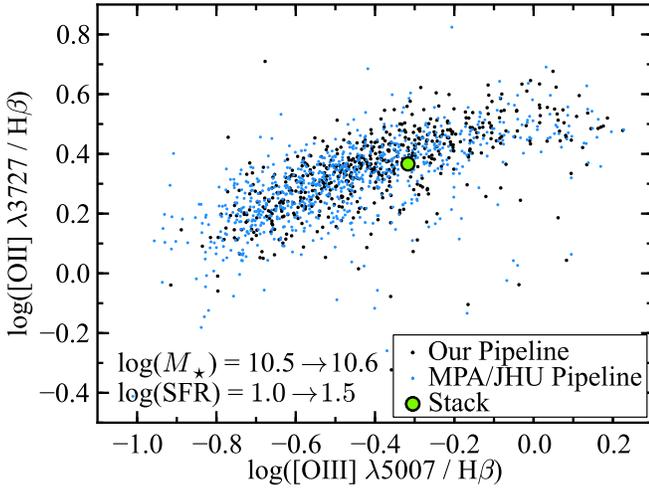
on SFR. They showed that the offset from the T_2–T_3 relation is likely due to the combined emission from multiple ionizing sources by comparing the observed T_e[O II]–T_e[O III] relation with the temperature predicted by H II region models that include ionizing sources of various temperatures. Based on these models, they concluded that differences in the hardness of the ionizing radiation, caused by the age-dependence of H II region spectral energy distributions, govern the scatter in the T_e[O II]–T_e[O III] plot for their sample of galaxies. Both our results and theirs suggest that galaxies with higher SFRs are more similar to the H II region models that served as the basis for the T_2–T_3 relation than galaxies with moderate SFRs. This is because they are more likely to be dominated by younger stellar populations that are better approximated by the input to the Stasińska (1982) models (see Section 3.1 for additional discussion).

The electron temperatures and metallicities of the stacks are unbiased relative to those of the input galaxies, but there is some evidence that the integrated galaxy electron temperature and metallicity are systematically higher and lower, respectively, than the electron temperatures and metallicities of the individual H II regions in the galaxy. Kobulnicky et al. (1999) compared the electron temperatures and metallicities of individual H II regions in a galaxy to the pseudo-global values derived by stacking the spectra of the individual H II regions. They showed that the electron temperatures and direct method metallicities of their galaxies were biased towards higher temperatures and lower metallicities by $\sim$1000–3000 K and 0.05–0.2 dex, respectively, relative to the median values of the individual H II regions. Global spectra are biased because they are the luminosity-weighted average of the H II regions, whose properties can vary widely (see, e.g., the large scatter around the T_2–T_3 relation for T_e measurements of individual H II regions in Figure 1 of Kennicutt et al. 2003 or Figure 4 of Izotov et al. 2006). The fluxes of the auroral lines might be particularly affected by a luminosity-weighted average because auroral line flux decreases non-linearly with metallicity. While Kobulnicky et al. (1999) only studied the effects on [O III] $\lambda4363$, the relative contribution of each H II region likely varies amongst the commonly measured ionic species, potentially yielding results that do not agree with the T_2–T_3 relation. We also note that their method of stacking H II regions does not perfectly simulate global line flux measurements because it does not account for the contribution of diffuse ionized gas (i.e., the emission from gas not in H II regions), which may affect the [N II] and [S II] line fluxes (see Moustakas & Kennicutt 2006). In summary, the differences in electron temperatures and metallicities between galaxy stacks and individual H II regions are dominated by the systematic offset between global galaxy properties and individual H II regions rather than any effects from stacking the global galaxy spectra.

The auroral lines are undetectable in high stellar mass galaxies, so we investigate the effect of stacking by comparing the oxygen strong line fluxes of individual galaxies to the stack of those galaxies. Figure 9 shows the [O II] $\lambda3727$ and [O III] $\lambda5007$ fluxes relative to Hβ for individual galaxies (small black and blue circles) with $\log(M_\star) = 10.5$–10.6 and $\log(\mathrm{SFR}) = 1.0$–1.5 and the stack of the same galaxies (large green circle). The small black and blue circles correspond to the line fluxes determined with our pipeline and the MPA-JHU pipeline, respectively. The distribution of individual galaxies with fluxes measured by our pipeline and the MPA-JHU pipeline coincide well. In detail, the median

stacks and galaxies in the T_e[N II]–T_e[O III] plot (Figure 8b), but the paucity of [N II] $\lambda5755$ detections limits the usefulness of any strong conclusions based on T_e[N II]. Overall, the qualitative agreement between the electron temperatures of the stacks and galaxies, especially for T_e[O II] and T_e[S II], demonstrates that the offset from the T_2–T_3 relation for the stacks shown in Figure 3 is not an artifact of stacking.

The majority of the galaxies lie below the T_2–T_3 relation, as was previously shown Pilyugin et al. (2010). We find a similar result for the galaxies in the T_e[S II]–T_e[O III] relation. Galaxies with moderate SFRs ($\log[\mathrm{SFR}] \sim 0.0$) are preferentially further below the T_2–T_3 relation than galaxies with high SFRs ($\log[\mathrm{SFR}] \gtrsim 1.0$) in the T_e[O II]–T_e[O III] plot. A similar effect is also present in the $M_\star$–SFR stacks. Pilyugin et al. (2010) found that galaxies with lower excitation parameters and [O III] $\lambda5007$/Hβ flux ratios had larger offsets from the T_2–T_3 relation, which is consistent with our result based

Figure 9. [O II] $\lambda3727$ and [O III] $\lambda5007$ fluxes relative to Hβ of galaxies in one $M_\star$–SFR bin (log[$M_\star$] = 10.5–10.6 and log[SFR] = 1.0–1.5) and the stack of those galaxies. The small black and blue circles represent individual galaxies with fluxes measured with our pipeline and the MPA-JHU pipeline (T04), respectively. The large green circle corresponds to the stack of the same galaxies.

fluxes from our pipeline are 0.08 and 0.04 dex higher for [O III] $\lambda5007$ and [O II] $\lambda3727$, respectively, than the median fluxes from the MPA-JHU pipeline. The [O III] $\lambda5007$ and [O II] $\lambda3727$ fluxes of the stack are 0.09 and 0.01 dex higher, respectively, than the median of fluxes from our pipeline. Although the spread is large in the individual galaxies (>1 dex for both [O III] $\lambda5007$ and [O II] $\lambda3727$), the stack is representative of the typical line fluxes of individual galaxies that went into the stack.

We also note that many of our stacks contain far more galaxies than are needed to simply detect a given line, and thus are unlikely to be dominated by a few, anomalous galaxies. As an example, we estimate how many galaxies would need to be stacked for a detection of [O II] $\lambda\lambda7320, 7330$. If we assume that the uncertainty on the line flux decreases as $\sqrt{N_{galaxies}}$, the error on the measurement of any individual galaxy is $\sigma_{stack} * \sqrt{N_{galaxies}}$. We use a 5σ detection threshold, so the minimum number of galaxies needed to detect a line is $N = [(5\sigma)/\text{flux}]^2$. For the $M_{\star 9.5}^{9.6}$–SFR$_{0.0}^{0.5}$ stack, the minimum number of galaxies required to detect [O II] $\lambda\lambda7320, 7330$ is $N_{galaxies} = 40$, which is well below the actual number of galaxies (1996) in this stack.

5. THE MASS–METALLICITY RELATION AND MASS–METALLICITY–SFR RELATION

5.1. *The Mass–Metallicity Relation*

In Figure 10, we plot the MZR with direct method metallicities for the $M_\star$ stacks (circles). We fit the MZR for the $M_\star$ stacks (black line) with the asymptotic logarithmic formula suggested by Moustakas et al. (2011):

$$12+\log(\text{O/H}) = 12+\log(\text{O/H})_{asm} - \log\left(1 + \left(\frac{M_{TO}}{M_\star}\right)^\gamma\right),$$
(5)

where $12+\log(\text{O/H})_{asm}$ is the asymptotic metallicity, M_{TO} is the turnover mass, and γ controls the slope of the MZR. This functional form is preferable to a polynomial because polynomial fits can produce unphysical anticorrelations between mass and metallicity, particularly when extrapolated beyond

the mass range over which they were calibrated. The metallicities and fit parameters for the stacks are reported in Tables 3 and 4, respectively. For comparison, we show the robust cubic polynomial fits of eight strong line MZRs (colored lines) from Kewley & Ellison (2008) in Figure 10a. The T04, Z94 R_{23}, KK04 R_{23}, KD02 N2O2, and M91 R_{23} MZRs are based on theoretical calibrations, whereas the D02 N2, PP04 O3N2, and PP04 N2 MZRs are based on empirical calibrations. In Figure 10b, the solid, dashed, and dotted gray lines indicate the median, 68% contour, and 95% contour, respectively, of the T04 MZR.

The most prominent aspect of the direct method MZR is its extensive dynamic range in both stellar mass and metallicity. It spans three decades in stellar mass and nearly one decade in metallicity; this wide range is critical for resolving the turnover in metallicity with a single diagnostic that is a monotonic relation between line strength and metallicity. The broad range in galaxy properties includes the turnover in the MZR, which is the first time this feature has been measured with metallicities derived from the direct method. Our stacked spectra also extend the direct method MZR to sufficiently high masses that there is substantial overlap with strong line measurements, and we use this overlap to compare them.

The direct method MZR shares some characteristics with strong line MZRs but differs in important ways, as can be seen in Figure 10a. The low mass end of the direct method MZR starts at $\log(M_\star) = 7.4$, a full decade lower than the strong line MZRs. Nonetheless, naive extrapolations of the T04, D02, PP04, and PP04 MZRs are in reasonable agreement with our direct method MZR. At a stellar mass of $\log(M_\star) = 8.5$, the lowest stellar mass where strong line MZRs are reported, the direct method MZR is consistent with the T04 and the D02 MZRs. Above this mass, the direct method MZR and the D02 MZR diverge from the T04 MZR. At $\log(M_\star) = 8.9$, the direct method MZR turns over. By contrast, the strong line MZRs turns over at a much higher stellar mass ($\log[M_\star] \sim 10.5$): a significant difference that has implications for how the MZR is understood in a physical context, which we discuss in Section 7.4. At high mass, the direct method MZR is in good agreement with the empirical strong line calibration MZRs, but the theoretical T04, Z94, KK04, and KD02 strong line calibration MZRs are offset to higher metallicities by ~0.3 dex at $\log(M_\star) = 10.5$, the highest mass stack with detected auroral lines. Figure 10b shows the direct method MZR in relation to the scatter of the T04 MZR. The direct method MZR is slightly below the median T04 MZR at $\log(M_\star) = 8.5$, crosses the 16th percentile at $\log(M_\star) = 9.0$, and drops below the 2nd percentile at $\log(M_\star) = 9.9$.

At low masses ($\log[M_\star] = 7.4$–8.9; i.e., below the turnover), the direct method MZR scales as approximately O/H $\propto M_\star^{1/2}$. While a comparison over the same mass range is not possible for the T04 MZR, its low mass slope, as determined from $\log(M_\star) = 8.5$–10.5, is shallower with O/H $\propto M_\star^{1/3}$. The discrepancy in the low mass slopes between the direct method and the T04 MZRs could be reasonably explained by the difference in the mass ranges over which the slopes were measured if the MZR steepens with decreasing stellar mass (c.f., Lee et al. 2006). We note that the direct method and D02 MZRs have similar slopes and normalizations over a wide range in masses from $\log(M_\star) = 8.5$–10.0.

5.2. *Mass–Metallicity–SFR Relation*
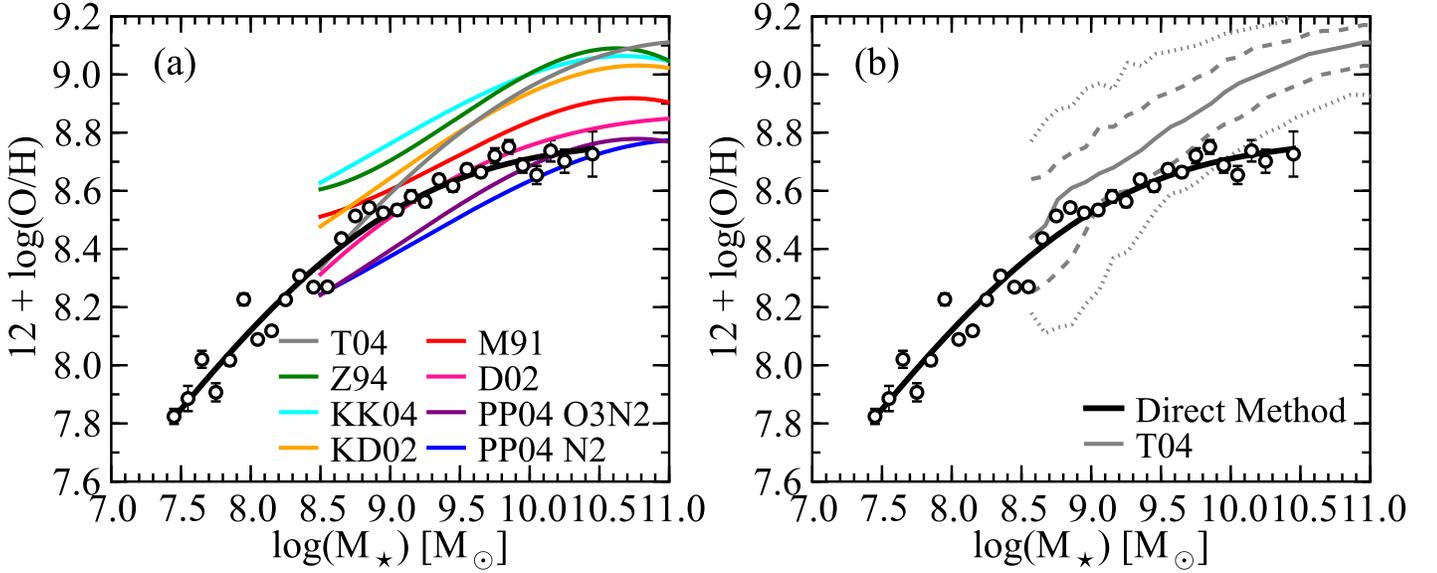
Figure 10. The direct method mass–metallicity relation for the $M_\star$ stacks (circles). In both panels, the thick black solid line shows the asymptotic logarithmic fit to the direct method measurements (see Equation 5). Panel (a): the colored lines represent various strong line calibrations (Tremonti et al. 2004; Zaritsky et al. 1994; Kobulnicky & Kewley 2004; Kewley & Dopita 2002; McGaugh 1991; Denicoló et al. 2002; Pettini & Pagel 2004). Panel (b): the solid, dashed, and dotted gray lines show the median, 68% contour, and 95% contour, respectively, of the Tremonti et al. (2004) MZR. The metallicities and fit parameters for the stacks are reported in Tables 3 and 4, respectively.

Table 4
Mass–Metallicity Relation Fit Parameters

Stacks SFR in $M_\odot$ yr^{-1} (1)	log($M_{\rm TO}$) [$M_\odot$] (2)	12+log(O/H)$_{\rm asm}$ [dex] (3)	γ (4)	Fit Range log($M_\star$) [$M_\odot$] (5)	Median log(O/H) Offset [dex] (6)
MZR	8.901	8.798	0.640	7.4–10.5	0.18
$-1.0 \leq$ log(SFR) < -0.5	8.253	8.726	0.734	7.2–9.7	0.15
$-0.5 \leq$ log(SFR) < 0.0	9.608	9.118	0.610	7.3–10.2	0.13
$0.0 \leq$ log(SFR) < 0.5	9.836	8.997	0.534	7.6–10.3	0.12
$0.5 \leq$ log(SFR) < 1.0	27.225	16.383	0.449	8.3–10.6	0.10
$1.0 \leq$ log(SFR) < 1.5	32.650	16.988	0.373	8.4–10.6	−0.04
$1.5 \leq$ log(SFR) < 2.0	28.369	16.259	0.438	9.5-10.8	0.04

Note. — Mass–Metallicity Relation given by $12 + \log(\rm O/H) = 12 + \log(\rm O/H)_{asm} - \log(1 + (M_{TO}/M_\star)^\gamma)$. Column (1): Stacks included in fits. MZR refers to $M_\star$ stacks. The SFR ranges refer to $M_\star$–SFR stacks. Column (2): Turnover mass. Column (3): Asymptotic metallicity. Column (4): Power-law slope. Column (5): Stellar mass range of each fit. Column (6): Median offset between the metallicity determined with (i) measured T_e[O II] and inferred T_e[O III] from the T_2–T_3 relation and (ii) measured T_e[O II] and measured T_e[O III] (see Section 3.2).

The features of the direct method MZR are shaped by the SFR-dependence of the MZR, which we investigate with the $M_\star$–SFR stacks. Figure 11 shows the $M_\star$–SFR stacks (circles color-coded by SFR) in the mass–metallicity plane (see Figure 1 for the number of galaxies per stack). The solid colored lines indicate the asymptotic logarithmic fits (Equation 5) of the $M_\star$–SFR stacks of a given SFR, hereafter referred to as SFR tracks (e.g., the orange line is the SFR$_{-1.0}^{-0.5}$ track). The solid black line is the direct method MZR of the $M_\star$ stacks from Figure 10; the solid, dashed, and dotted gray lines are the median, 68% contour, and 95% contour, respectively, of the T04 MZR. The error bars represent the mean error for the $M_\star$–SFR stacks of a given SFR.

The $M_\star$–SFR stacks help establish the robustness of the direct method MZR. The low turnover mass and metallicity of the direct method MZR relative to the T04 and other theoretical strong line calibration MZRs is reminiscent of empirical strong line calibration MZRs that suffer from a lack of sensitivity at high metallicities. However, the most metal-rich $M_\star$–SFR stacks have some of the highest direct method metallicities ($12 + \log[\rm O/H] > 9.0$)—metallicities well above the turnover metallicity of the direct method MZR. These measurements unambiguously demonstrate that the turnover in the direct method MZR is not caused by a lack of sensitivity to high metallicities.

The $M_\star$–SFR stacks also can be used to test if galaxies with the highest SFRs at a given stellar mass disproportionately influence the line fluxes and metallicities of the $M_\star$ stacks. High SFR galaxies have more luminous emission lines and lower metallicities and thus may dominate the inferred metallicity of the stack. To investigate this possibility, we calculated the difference between the metallicity of the $M_\star$ stack and the
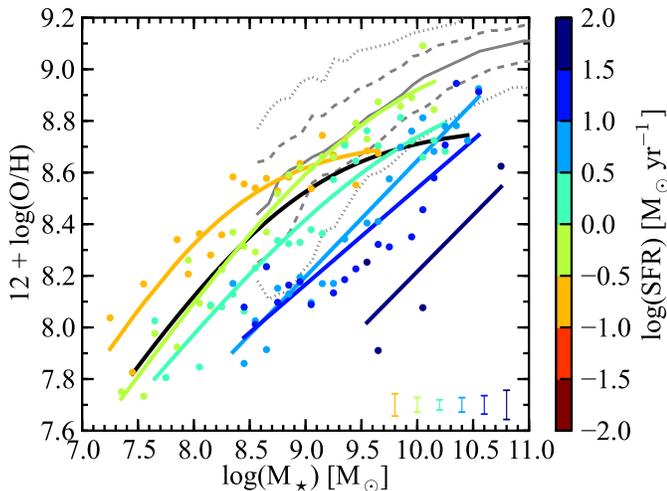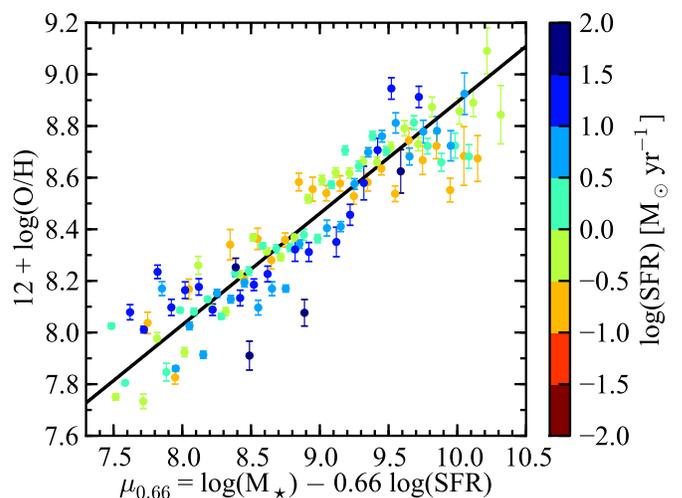
Figure 11. The direct method $M_\star$–Z–SFR relation for the $M_\star$–SFR stacks (circles color-coded by SFR) in the mass–metallicity plane. The thick solid lines color-coded by SFR show the asymptotic logarithmic fits (see Equation 5) for the $M_\star$–SFR stacks. The thick black line shows the direct method MZR from Figure 10. The solid, dashed, and dotted gray lines show the median, 68% contour, and 95% contour, respectively, of the Tremonti et al. (2004) MZR. The error bars correspond to the mean error for the $M_\star$–SFR stacks of a given SFR. The metallicities and fit parameters for the stacks are given in Tables 3 and 4, respectively.

Figure 12. The direct method fundamental metallicity relation for the $M_\star$–SFR stacks (circles color-coded by SFR). The coefficient (0.66) on log(SFR) in the abscissa minimizes the scatter in the FMR (see Equation 1). The black line shows a linear fit to the data, with a slope of 0.43.

galaxy number-weighted average of the metallicities of the $M_\star$–SFR stacks (for the stacks with measured metallicities) at a given stellar mass. The median offset is only −0.037 dex in metallicity; for reference, the median metallicity uncertainties for the $M_\star$ and $M_\star$–SFR stacks are 0.019 and 0.027 dex, respectively. The slight offset could be due to preferentially including the metallicities of $M_\star$–SFR stacks with higher SFR (lower metallicity) relative to lower SFR (higher metallicity) in the weighted average because the former tend to have larger line fluxes than the latter, whereas the $M_\star$ stacks include the contribution from galaxies of all SFRs at a given stellar mass. Still, the magnitude of this offset is small, which indicates that the highest SFR galaxies do not have an appreciable effect on the metallicity of the $M_\star$ stacks because they are quite rare (see Figure 1). Furthermore, the metallicities of the $M_\star$ stacks effectively track the metallicity of the most common galaxies at a given stellar mass.

The most striking features of Figure 11 are the 0.3–0.6 dex offsets in metallicity at fixed stellar mass between the $M_\star$–SFR stacks. This trend results from the substantial, nearly monotonic dependence of the MZR on SFR. At a given stellar mass, higher SFR stacks almost always have lower metallicities than lower SFR stacks, so there is little overlap between the different SFR tracks. Furthermore, the small regions with overlap may be the result of the observational uncertainties.

The interplay between stellar mass, SFR, and metallicity for typical galaxies is reflected in the features of the direct method MZR, especially the turnover mass. The constant SFR tracks (colored lines in Figure 11) show that metallicity increases with stellar mass at fixed SFR. However, the typical SFR also increases with stellar mass, which shifts the "typical" galaxy (as measured by the $M_\star$ stacks) to progressively higher SFR and consequently lower metallicity at fixed stellar mass. Taken together, the turnover in the MZR is the result of the conflict between the trend for more massive galaxies to have higher SFRs and the trend for metallicity to decrease with SFR at fixed mass. The turnover in the T04 MZR (and

other strong line calibration MZRs) occurs at a higher stellar mass than the the direct method MZR because the strong line metallicity calibrations produce a weaker SFR–metallicity anticorrelation. This means that the progression to higher SFRs with increasing stellar mass has less of an effect on the MZR.

Interestingly, the $SFR^{0.0}_{-0.5}$ stacks (light green circles/line) are nearly identical to the T04 MZR in slope, shape, turnover, and normalization. While the exact cause of this agreement is unclear, it is possible that the photoionization models that underlie the T04 metallicities assume physical parameters that are most appropriate for galaxies with this range of SFR. We discuss potential systematic effects of strong line calibrations in Section 7.3.

The stacks with very high SFRs ($SFR^{1.5}_{1.0}$ and $SFR^{2.0}_{1.5}$; blue and dark blue circles/lines, respectively) have significantly lower metallicities than the stack of all galaxies at fixed mass in the MZR. The high SFRs and low metallicities of these galaxies suggests that they are probably undergoing major mergers, as found by Peeples et al. (2009) for similar outliers. Major mergers drive in considerable amounts of low metallicity gas from large radii, which dilutes the metallicity of the galaxy and triggers vigorous star formation (e.g., Kewley et al. 2006, 2010; Torrey et al. 2012). These stacks also have a larger scatter than lower SFR stacks, which is likely driven by the small numbers of galaxies per stack coupled with the large intrinsic dispersion in the individual galaxy metallicities.

5.3. The Fundamental Metallicity Relation

The orientation of the $M_\star$–Z–SFR relation captures the importance of SFR as a second parameter to the MZR (Lara-López et al. 2010; Mannucci et al. 2010). Mannucci et al. (2010) established the convention that the FMR is the projection of least scatter found by choosing a free parameter α that minimizes the scatter in the metallicity vs. $\mu_\alpha \equiv \log(M_\star) - \alpha \log(SFR)$ plane (Equation 1). Mannucci et al. (2010) found a value of $\alpha = 0.32$ for a sample of SDSS galaxies with metallicities determined with the semi-empirical calibration of Maiolino et al. (2008). As metallicity estimates are well known to vary substantially between different methods, the parameter α may also be different due to potentially different correlations between the inferred metal-

Table 5
Best Fit α

Calibration (1)	α (2)
direct method	0.66
KK04	0.24
M91	0.17
Z94	0.25
KD02	0.12
D02	0.34
PP04 N2	0.30
PP04 O3N2	0.32

Note. — Column (1): Metallicity calibration (see Section 3.3 for a more detailed description of the strong line calibrations). Column (2): The coefficient on log(SFR) in Equation (1) that minimizes the scatter in the fundamental metallicity relation.

licity and the SFR. For example, Yates et al. (2012) used the T04 metallicities, rather than those employed by Mannucci et al. (2010), and found a lower value of $\alpha = 0.19$.

Figure 12 shows the fundamental metallicity relation for the $M_\star$–SFR stacks (circles color-coded by SFR). The scatter in metallicity at fixed μ_α is minimized for $\alpha = 0.66$, which is significantly larger than the α values found by Mannucci et al. (2010) and Yates et al. (2012) for metallicities estimated with strong line calibrations. The scatter for the stacks differs from the scatter for individual galaxies (like the Mannucci et al. 2010 and Yates et al. 2012 studies) because the number of galaxies per stack varies. For a direct comparison, we computed the value of α for the metallicities derived from various empirical, semi-empirical, and theoretical strong line calibrations for the stacks with log(SFR) > -1.0 (the same SFR range as the stacks with direct method metallicities) and find low α values ($\alpha = 0.12$–0.34) that are consistent with the Mannucci et al. (2010) and Yates et al. (2012) α values (see Table 5). The significant difference in α between the direct method and the strong line methods indicates that the calibrations of all of the strong line methods have some dependence on physical properties that correlate with SFR.

The scatter in the direct method FMR ($\sigma = 0.13$) is almost a factor of two smaller than the scatter in the direct method MZR ($\sigma = 0.22$). This decrease is due to two features of the $M_\star$–SFR stacks at fixed SFR shown as the solid colored lines in Figure 11: (1) they are substantially offset from one another; (2) they have similar slopes with minimal overlap. The former reflects a strong SFR-dependence on the MZR; the latter corresponds to a monotonic SFR–metallicity relation at fixed stellar mass.

Figure 13 shows the $M_\star$–SFR stacks (circles color-coded by SFR) in the mass–metallicity plane with metallicities determined with two representative strong line calibrations: the Kobulnicky & Kewley (2004) theoretical R_{23} calibration (panel a) and the Pettini & Pagel (2004) empirical N2 calibration (panel b). Only stacks with log($M_\star$) ≥ 8.0 were included

in Figure 13 because some stacks at lower stellar masses had unphysically high strong line metallicities; to facilitate comparison with Figure 11, only stacks with log(SFR) > -1.0 are shown in Figure 13. The stacks in panel (a) show the metallicity from the upper branch of R_{23}, which were selected to have log([N II] $\lambda 6583/H\alpha$) > -1.1 (Kewley & Ellison 2008). Panel (b) shows stacks with $-2.5 < \log$([N II] $\lambda 6583/H\alpha$) < -0.3, the calibrated range for the Pettini & Pagel (2004) N2 calibration according to Kewley & Ellison (2008). For reference, the thick black line shows the direct method MZR. The median, 68% contour, and 95% contour of the T04 MZR are indicated by the solid, dashed, and dotted gray lines, respectively.

The scatter in metallicity about the best fit relation decreases only marginally from the MZR to the FMR when strong line calibrations are used to estimate metallicity. For the KK04 and PP04 N2 metallicities, the scatter is reduced by $\sigma = 0.10 \rightarrow 0.09$ and $\sigma = 0.10 \rightarrow 0.07$, respectively. Figure 13 also shows that the constant SFR tracks for the strong line calibrations in the mass–metallicity plane are both more closely packed and overlap more than those of the direct method. Figure 13 only shows the $M_\star$–SFR stacks with metallicities from two strong line calibrations, one theoretical and one empirical, but the minor reduction in scatter, small spread, and considerable overlap are generic features of strong line metallicities (the normalization is not).

A qualitative measure of the spread is the difference between the metallicity of the SFR$_{-0.5}^{0.0}$ (light green) and the SFR$_{0.5}^{1.0}$ (light blue) stacks at a given stellar mass. There are 17 stellar mass bins with direct method metallicities for stacks with these SFRs. The median metallicity difference for these pairs of stacks was 0.38 dex for the direct method, 0.15 dex for the Kobulnicky & Kewley (2004) calibration, and 0.13 dex for the Pettini & Pagel (2004) calibration. The factor of $\sim$2–3 difference between the direct method and strong line metallicities translates into an analogous difference in the SFR-dependence of the MZR.

Another feature of the strong line MZRs at fixed SFR is that different SFR tracks turn over at different stellar masses. Low SFR tracks turn over at lower stellar masses than high SFR tracks, so the sign of the dependence of the MZR on SFR changes with stellar mass. At low stellar masses, higher SFR stacks have lower metallicities; at high stellar masses, the opposite is true—higher SFR stacks have higher metallicities. Yates et al. (2012) found a similar, but more dramatic, result for their sample of galaxies that used T04 metallicities. The origin of the weak SFR-dependence and non-monotonic relation for the strong line calibrations is not obvious, but we discuss several potentially relevant effects in Section 7.3.

6. N/O ABUNDANCE

Nitrogen provides interesting constraints on chemical evolution because it is both a primary and secondary nucleosynthetic product. The yields of primary elements are independent of the initial metal content of a star but the yields of secondary elements are not. In a low metallicity star, the majority of the seed carbon and oxygen nuclei that will form nitrogen during the CNO cycle are created during helium burning in the star, so the nitrogen yield of such a star will scale roughly with the carbon and oxygen yields. In this case, carbon, nitrogen, and oxygen all behave like primary elements. After the ISM becomes sufficiently enriched, the nitrogen yield of a star principally depends on the amount of carbon and oxygen incorporated in the star at birth. The carbon and oxygen still behave like primary elements, but nitrogen is a secondary
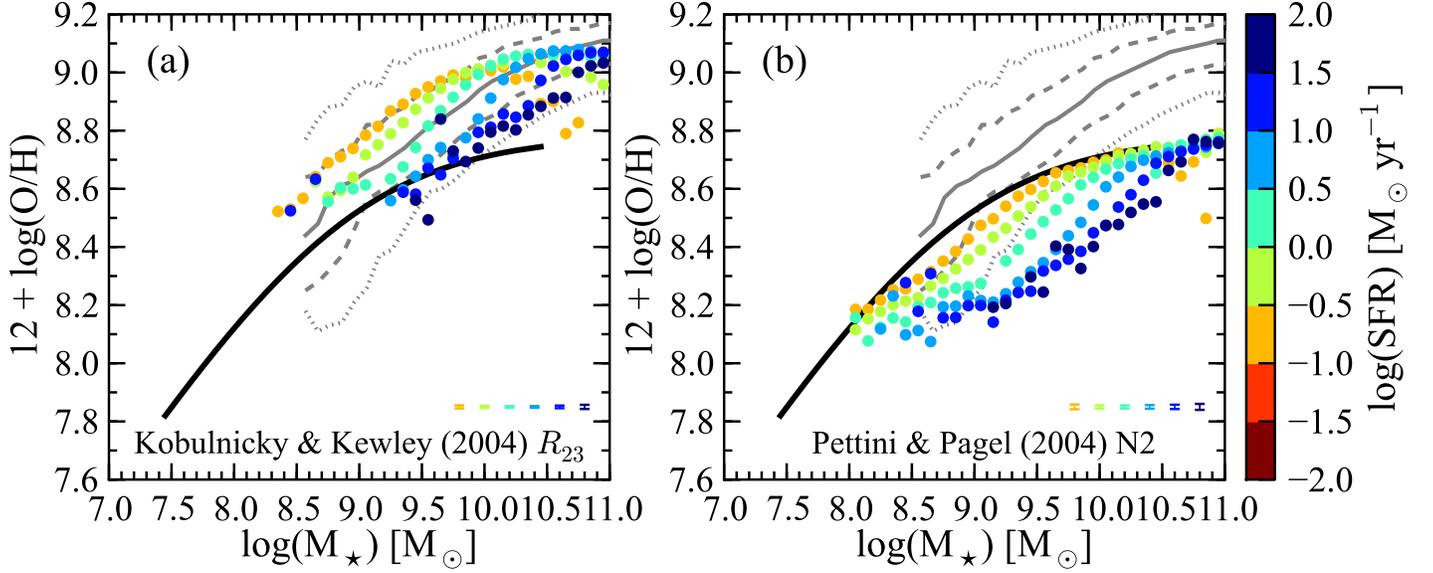
Figure 13. The $M_\star$–SFR stacks (circles color-coded by SFR) in the mass–metallicity plane with metallicities determined with the Kobulnicky & Kewley (2004) R_{23} calibration (panel a) and the Pettini & Pagel (2004) N2 calibration (panel b). The thick black line shows the direct method MZR from Figure 10. The solid, dashed, and dotted gray lines show the median, 68% contour, and 95% contour, respectively, of the Tremonti et al. (2004) MZR. The error bars correspond to the mean error for the $M_\star$–SFR stacks of a given SFR.
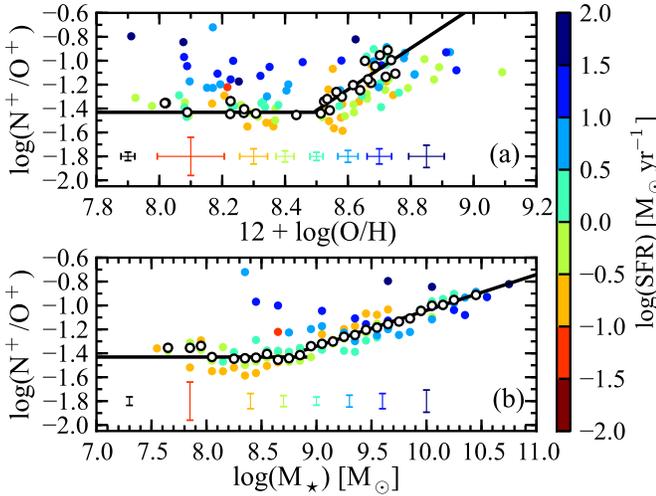
Figure 14. N^+/O^+ ratio as a function of direct method oxygen abundance (panel a) and $M_\star$ (panel b) for the $M_\star$ stacks (open circles) and $M_\star$–SFR stacks (circles color-coded by SFR). The horizontal lines show the median of the low oxygen abundance ($12 + \log(O/H) < 8.5$) and low stellar mass ($\log[M_\star] < 8.9$) data. The positively sloped lines in panels (a) and (b) are linear fits to the stacks with $12 + \log(O/H) > 8.5$ and $\log(M_\star) > 8.9$, respectively, whose fit parameters are given in Table 6. The error bars show the mean error for the $M_\star$ stacks (black) and each SFR bin of the $M_\star$–SFR stacks (color-coded by SFR). If N^+/O^+ is assumed to trace N/O, as is often done, then our results can be compared directly to literature results on N/O. The N/O abundances of the stacks are reported in Table 3.

nucleosynthetic product. Observational studies (Vila Costas & Edmunds 1993; van Zee & Haynes 2006; Berg et al. 2012) have found clear evidence for primary and secondary nitrogen at low and high metallicity. Vila Costas & Edmunds (1993) created a simple, closed box chemical evolution model that quantified the regimes where nitrogen is expected to behave like a primary and secondary element. However, modeling nitrogen enrichment is difficult because of the large uncertainties in stellar yields and the delay time for nitrogen enrichment relative to oxygen. Galactic winds also complicate nitrogen

enrichment because they may preferentially eject oxygen relative to nitrogen (van Zee & Haynes 2006). This is because oxygen is formed quickly in massive stars and is available to be ejected from galaxies by winds associated with intense bursts of star formation. By contrast, the >100 Myr delay before the release of nitrogen from intermediate mass AGB stars might be sufficient to protect it from ejections by a galactic winds.

The N/O abundance as a function of oxygen abundance can be used to disentangle the effects of nucleosynthesis, galactic inflows and outflows, and different star formation histories on the relative enrichment of nitrogen. The total N/O ratio is a difficult quantity to measure because [N III] lines are not readily observable, so N^+/O^+ is used frequently as a proxy for N/O. This assumption is supported by the photoionization models of Garnett (1990), which showed that the ionization correction factor from N^+/O^+ to N/O should be ∼1 to within 20%. Because the ionization factor should be close to unity, most papers in the literature (e.g., Vila Costas & Edmunds 1993) that show N/O have assumed N/O = N^+/O^+. For transparency, we plot N^+/O^+ as a function of direct method oxygen abundance in Figure 14a for the $M_\star$ and $M_\star$–SFR stacks. We measured the ionic abundances of N^+ and O^+ with the direct method under the assumption that T_e[O II] represents T_2 (see Section 3.2).

At low metallicity ($12 + \log(O/H) < 8.5$), we find that the $M_\star$ stacks have an approximately constant value of N^+/O^+, which is expected for primary nitrogen. These stacks have a median of $\log(N^+/O^+) = -1.43$ (indicated by the horizontal line[5]), which is consistent with other studies of H II regions and dwarf galaxies (Vila Costas & Edmunds 1993). At $12 + \log(O/H) = 8.5$, there is a sharp transition where N^+/O^+ increases steeply with oxygen abundance (slope = 1.73), which shows that nitrogen is acting like a secondary element.

---

[5] We do not show a fit to these points because of the strong *a priori* expectation of a constant N^+/O^+ at low metallicity (and low mass); however, a linear fit would have a slope of −0.21. The analogous slope for the low mass N^+/O^+–$M_\star$ relation is −0.08.

**Table 6**
N/O vs. O/H and $M_\star$ Fit Parameters for $M_\star$ Stacks

Abscissa (1)	Slope (2)	y-intercept (3)	Dispersion (4)	Fit Range (5)
$12 + \log(\mathrm{O/H})$	0	-1.43	0.04	$12 + \log(\mathrm{O/H}) < 8.5$
$12 + \log(\mathrm{O/H})$	1.73	-16.15	0.08	$12 + \log(\mathrm{O/H}) > 8.5$
$M_\star$	0	-1.43	0.04	$M_\star < 8.9$
$M_\star$	0.30	-4.04	0.01	$M_\star > 8.9$

Note. — Column (1): N/O as a function of $12 + \log(\mathrm{O/H})$ or $M_\star$. Column (2): Slope of linear fit (set to 0 for first and third rows). Column (3): y-intercept of linear fit. Column (4): Dispersion around fit. Column (5): Range in $12 + \log(\mathrm{O/H})$ or $M_\star$ of the fit.

Previous observations (e.g., Vila Costas & Edmunds 1993) have found a smoother transition between primary and secondary nitrogen and a shallower slope in the secondary nitrogen regime, albeit with large dispersion that could be obscuring these features. The fit parameters of the $\mathrm{N^+/O^+}$–O/H relation for the $M_\star$ stacks is presented in Table 6.

The $M_\star$ stacks form a tight sequence with a dispersion of only $\sigma = 0.08$, compared to a more typical dispersion of $\sigma \sim 0.3$ for individual objects (e.g., Henry et al. 2000). A plausible explanation for the additional scatter in the N/O–O/H relation for individual galaxies is the time-dependence of N/O caused by the difference in enrichment timescales of oxygen and nitrogen following a burst of star formation. The $M_\star$–SFR stacks show a larger dispersion than the $M_\star$ stacks, potentially because these stacks contain fewer galaxies. The low and moderate SFR stacks ($\mathrm{SFR}_{-1.0}^{-0.5}$, $\mathrm{SFR}_{-0.5}^{0.0}$, and $\mathrm{SFR}_{0.0}^{0.5}$) follow the general trend of the $M_\star$ stacks; however, the high SFR stacks ($\mathrm{SFR}_{0.5}^{1.0}$, $\mathrm{SFR}_{1.0}^{1.5}$, and $\mathrm{SFR}_{1.5}^{2.0}$) have higher $\mathrm{N^+/O^+}$ at a given oxygen abundance, which may be because these galaxies have experienced a large inflow of gas that would lower O/H at fixed N/O (i.e., move galaxies to the left in Figure 14a). Another consequence of a vigorous burst of star formation is the production of Wolf-Rayet stars that can enrich the gas in nitrogen for a brief period before the oxygen enrichment from the subsequent SNe II (Berg et al. 2011). We see evidence for Wolf-Rayet features, such as He II $\lambda4686$, in some of our stacks, especially at low mass.

Some of the features in the $\mathrm{N^+/O^+}$–O/H relation are clarified by the associated relation between $\mathrm{N^+/O^+}$ and stellar mass, which is shown in Figure 14b for the $M_\star$ and $M_\star$–SFR stacks (see Table 6 for the fit parameters of the $\mathrm{N^+/O^+}$–$M_\star$ relation for the $M_\star$ stacks). Similar to Figure 14a, there is a primary nitrogen plateau in $\mathrm{N^+/O^+}$ at low stellar mass ($\log[M_\star] < 8.9$) and a steady increase in $\mathrm{N^+/O^+}$ due to secondary nitrogen enrichment above $\log(M_\star) = 8.9$ (slope = 0.30). However, in the secondary nitrogen regime, the $\mathrm{N^+/O^+}$–$M_\star$ relation has a much lower dispersion ($\sigma = 0.01$) than the $\mathrm{N^+/O^+}$–O/H relation ($\sigma = 0.08$). Some of the decreased dispersion is due to the larger dynamic range of stellar mass relative to oxygen abundance, but the tightness of the $\mathrm{N^+/O^+}$–$M_\star$ relation suggests that the enrichment of nitrogen relative to oxygen is well-behaved on average. The essentially zero intrinsic dispersion in the $\mathrm{N^+/O^+}$–$M_\star$ relation can be used to quantify the effect of gas inflow and galactic winds on enrichment if all of the scatter in $\mathrm{N^+/O^+}$ at a given O/H is due to gas flows into and out of galaxies. As in the $\mathrm{N^+/O^+}$–O/H relation, the low and moderate SFR stacks ($\mathrm{SFR}_{-1.0}^{-0.5}$, $\mathrm{SFR}_{-0.5}^{0.0}$, and $\mathrm{SFR}_{0.0}^{0.5}$) roughly coincide with the $M_\star$ stacks. The high SFR stacks ($\mathrm{SFR}_{0.5}^{1.0}$,
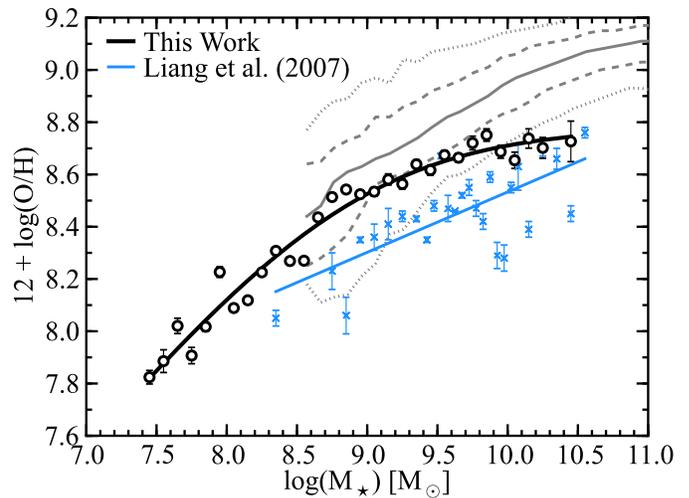
Figure 15. Our direct method MZR (open circles and thick black line) and the Liang et al. (2007) direct method MZR (blue crosses and line). For reference, the solid, dashed, and dotted gray lines show the median, 68% contour, and 95% contour, respectively, of the Tremonti et al. (2004) MZR.

$\mathrm{SFR}_{1.0}^{1.5}$, and $\mathrm{SFR}_{1.5}^{2.0}$) still tend to be more nitrogen enriched than the $M_\star$ stacks at a fixed $M_\star$, but the discrepancy has decreased. The $\mathrm{N^+/O^+}$–$M_\star$ diagram is less sensitive to dilution (traced by SFR) because the high SFR galaxies with low O/H are less significant outliers when shown as a function of stellar mass.

The N/O–$M_\star$ relation has been previously investigated by Pérez-Montero & Contini (2009) and Perez-Montero et al. (2012), who used strong line methods to estimate N/O. They found that N/O increased steadily with stellar mass and did not show a plateau at low stellar mass associated with primary nitrogen enrichment, in contrast to the direct method N/O–$M_\star$ relation. However, Perez-Montero et al. (2012) showed that the strong line N/O–$M_\star$ relation is nearly independent of SFR, which is roughly consistent with our finding that the N/O–$M_\star$ relation has only a mild dependence on SFR, particularly at $\log(M_\star) \gtrsim 9.0$.

7. DISCUSSION

7.1. Comparison to a Previous Analysis That Used Auroral Lines from Stacked Spectra

Liang et al. (2007) stacked SDSS spectra and applied the direct method to estimate the MZR, although their study differs from ours in a number of important respects. First, their study is based on DR4 spectroscopy of 23,608 galaxies, which is approximately an order of magnitude fewer than our sample. Second, they implemented a minimum [O II] $\lambda3727$ EW criterion to select the input galaxies to their stacks in order to increase the SNR of their stacked spectra. Finally, they only measured T_e[O II] from the [O II] $\lambda\lambda7320, 7330$ lines and then inferred T_e[O III] (and the $\mathrm{O^{++}}$ ionic abundance) from the T_2–T_3 relation provided by Izotov et al. (2006). These differences are likely responsible for the offset between our MZR and the Liang et al. (2007) MZR, the absence of a turnover in their MZR, and their greater scatter as shown in Figure 15.

The [O II] selection criterion can readily explain part of the offset between our MZRs. Liang et al. (2007) only selected galaxies with above average [O II] $\lambda3727$ EW (at fixed mass) for galaxies with $\log(M_\star) < 10$ and required a more stringent EW([O II]) > 30 Å for galaxies with $\log(M_\star) > 10$. As a result of this selection, their stacks have systematically higher

SFRs by approximately 0.15 to 0.2 dex. This in turn biases the stacks to lower metallicities because of the $M_\star$–Z–SFR relation (Mannucci et al. 2010; Lara-López et al. 2010). The magnitude of this effect ($\sim$0.05–0.08 dex) accounts for part of the difference between the MZRs. Another effect of this selection is that the increase in average SFR increases the turnover mass and makes it less distinct (see Figure 11).

The turnover mass is also not apparent in their MZR due to the greater scatter, which is largely due to their order of magnitude smaller sample. The scatter around the linear fit from $\log(M_\star)$ = 8.0–10.5 for their data is $\sigma = 0.12$. The scatter around an asymptotic logarithmic fit (Equation 5) is reduced only to $\sigma = 0.11$. An asymptotic logarithmic fit has an additional degree of freedom relative to a linear fit, so the marginal improvement in σ suggests that the Liang et al. (2007) MZR can be sufficiently characterized by a linear fit. Over the same mass range, the scatter around the asymptotic logarithmic fit of our data (thick black line) is only $\sigma = 0.03$, or a factor of four smaller. The smaller scatter in our MZR enables a clear identification of the turnover.

The method employed by Liang et al. (2007) to estimate the oxygen abundance is also distinct from ours and may explain the rest of the discrepancy in the normalization difference between our studies. The Liang et al. (2007) study relies solely on the [O II] $\lambda\lambda7320$, 7330 auroral lines to measure T_e[O II], which is used to infer T_e[O III] and the O^{++} abundance by applying the T_2–T_3 relation and T_e[O III]–(O^{++}/H^+) formula from Izotov et al. (2006). They did not detect [O III] $\lambda4363$ in their stacks, which they only binned in stellar mass, because they had fewer galaxies per bin. The stellar continuum subtraction may also have affected the detection of [O III] $\lambda4363$ because of its proximity to the Hγ stellar absorption feature, whereas the stellar continuum is comparatively featureless in the vicinity of the [O II] $\lambda\lambda7320$, 7330 lines. Liang et al. (2007) used the Bruzual & Charlot (2003) spectral templates, rather than the empirical and higher resolution MILES templates that we have adopted (see Section 2.3), and this difference may also have played an important role. As a consequence of their lack of a detection of [O III] $\lambda4363$, their oxygen abundance estimate depends on the quality of the assumption that the galaxies obey the T_2–T_3 relation of Izotov et al. (2006). Our empirical measurements of T_2 and T_3 indicate that this assumption underestimates T_3 and overestimates O^{++}/H, which may partly explain why our MZRs are in better agreement at high mass where O^+ is the dominant ionization state of oxygen.

7.2. *Temperature and Metallicity Discrepancies*

Temperatures and metallicities of H II regions measured with the direct method do not always agree with those measured with other techniques. For example, temperatures measured with the direct method tend to be systematically higher than those measured from the Balmer continuum (Peimbert 1967). Also, the metallicities determined from optical recombination lines (e.g., C II $\lambda4267$ and O II $\lambda4649$) and far-IR fine-structure lines (e.g., [O III] 52, 88 μm) tend to be 0.2–0.3 dex higher than those from collisionally excited lines (García-Rojas & Esteban 2007; Bresolin 2008; Esteban et al. 2009). The exact cause of these temperature and abundance discrepancies is currently not understood.

Peimbert (1967) proposed that temperature fluctuations and gradients in H II regions cause direct method temperatures to be systematically overestimated, while direct method metallicities are underestimated. To account for temperature variations across a nebula, he introduced the concept of t^2, the root mean square deviation of the temperature from the mean. Estimating t^2 has proven to be difficult, so most direct method metallicity studies assume $t^2 = 0$. However, optical recombination lines and far-IR fine-structure lines are less sensitive to temperature than collisionally excited lines, so they could be used to estimate t^2 if the discrepancy between the metallicity determined from collisionally excited lines and optical recombination lines or far-IR fine-structure lines is assumed to be caused by temperature fluctuations. The few studies that have measured optical recombination lines (e.g., García-Rojas & Esteban 2007; Esteban et al. 2009) find that values of $t^2 = 0.03$–0.07 are necessary to increase the direct method metallicities by 0.2–0.3 dex to match the optical recombination line metallicities.

Recently, Nicholls et al. (2012) suggested that the electron energy distribution could be the cause of the temperature and metallicity discrepancies. Specifically, they questioned the widespread assumption that the electrons are in thermal equilibrium and can be described by a Maxwell-Boltzmann distribution. Instead, they suggested that a there might be an excess of high energy electrons and proposed that a κ-distribution is a more appropriate description of the electron energy distribution. The κ-distribution is based on direct measurements of solar system plasmas. Assuming a κ-distribution for an H II region lowers the derived temperature, increases the inferred metallicity, and could potentially resolve the discrepancy between the temperatures and metallicities found with optical recombination lines and collisionally excited lines.

Models of H II regions by Stasińska (2005) indicate that metallicities based on the direct method could suffer from systematic biases in metal-rich H II regions. She finds that measuring metallicity from T_e[O III] and T_e[N II] tends to dramatically underestimate the true metallicity for $12 + \log(O/H) > 8.6$ (see her Figure 1). The situation does not improve if metallicities are computed with only T_e[N II] because the derived metallicity can wildly overestimate or underestimate the true metallicity depending on the physical conditions and geometry of the H II region. However, there are two key differences between the models of Stasińska (2005) and the measurements made in this study that could minimize the bias. First, we measured the temperature of the low ionization region from T_e[O II], not T_e[N II]. Second, we analyzed spectra of galaxy stacks and not individual H II regions, which may average out the large predicted errors. Our stacks generally increase smoothly in metallicity as a function of $M_\star$, which does not rule out systematic error but minimizes the impact of the individual, catastrophic errors highlighted in Stasińska (2005).

7.3. *Strong Line Calibrations and the SFR-dependence of the FMR*

The MZRs and FMRs based on strong line calibrations (Figure 13) have a much weaker dependence on SFR than the direct method MZR and FMR (Figures 10–12). Relative to the direct method MZR and FMR, the strong line MZR and FMR have (1) a smaller spread in the mass–metallicity plane (compare Figures 11 and 13), (2) a smaller reduction in scatter from the MZR to the FMR (see Section 5.3), and (3) a smaller value of α (see Table 5). This trend is a generic feature of strong line calibrations that holds for both empirical and theoretical calibrations and for all strong line indicators (R_{23}, N2, N2O2, and O3N2) that we used. Since a strong line calibration is only applicable to the physical conditions
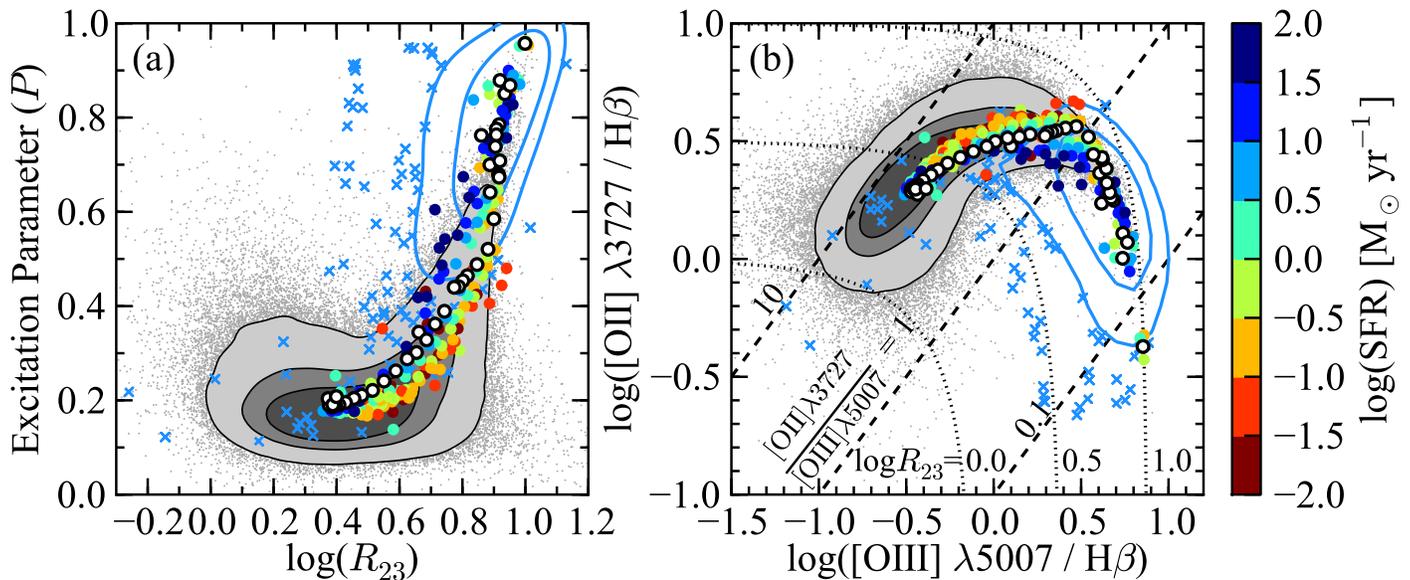
Figure 16. Panel (a) shows the excitation parameter, $P =$ [O III] $\lambda\lambda$4959, 5007 / ([O II] λ3727 + [O III] $\lambda\lambda$4959, 5007), as a function of $R_{23} =$ ([O II] λ3727 + [O III] $\lambda\lambda$4959, 5007) / Hβ. Panel (b) shows log([O II] λ3727 / Hβ) versus log([O III] λ5007 / Hβ). The gray scale contours (50%, 75%, and 95%) and gray points correspond to SDSS star-forming galaxies. The white and colored circles represent the $M_\star$ and $M_\star$–SFR (color-coded by SFR) stacks, respectively. The light blue contours (50% and 75%) and light blue crosses show H II regions with direct method metallicities from the Pilyugin et al. (2012) compilation. In panel (b), the dashed and dotted lines show lines of constant [O II] λ3727 / [O III] λ5007 and R_{23}, respectively. The stacks trace the overall galaxy distribution better than H II regions, especially at lower excitation parameters. The H II regions tend to have high excitation parameters because the auroral line flux is a strong function of metallicity and hence R_{23}.

spanned by the calibration sample or model, it is important to understand the physical properties of the calibration sample for empirical calibrations and the assumptions behind the H II region models that underlie theoretical calibrations.

Figure 16 compares excitation parameter (P) and R_{23} (panel a) and [O II] and [O III] fluxes relative to Hβ (panel b) for galaxies, stacks of galaxies, and H II regions. The gray contours (50%, 75%, and 95%) and points indicate SDSS star-forming galaxies, whose line flux measurements come from the MPA-JHU catalog (Tremonti et al. 2004), after we corrected their measured values for intrinsic reddening. The stacks are shown by the open and colored circles. Extragalactic H II regions with direct method metallicities are represented by the light blue contours and crosses. The dereddened line fluxes of the H II regions come from the literature compilation by Pilyugin et al. (2012)[6].

[6] The original data can be found in Bresolin et al. (2004), Bresolin et al. (2005), Bresolin (2007), Bresolin et al. (2009a), Bresolin et al. (2009b), Campbell et al. (1986), Castellanos et al. (2002), de Blok & van der Hulst (1998), Esteban et al. (2009), Fierro et al. (1986), French (1980), Fricke et al. (2001), Garnett et al. (1997), Garnett et al. (2004), Gonzalez-Delgado et al. (1994), Guseva et al. (2000), Guseva et al. (2001), Guseva et al. (2003a), Guseva et al. (2003b), Guseva et al. (2004), Guseva et al. (2009), Guseva et al. (2011), Hägele et al. (2008), Hawley (1978), Hodge & Miller (1995), Izotov et al. (1994), Izotov et al. (1997), Izotov & Thuan (1998a), Izotov & Thuan (1998b), Izotov et al. (1999), Izotov et al. (2001), Izotov et al. (2004), Izotov & Thuan (2004), Izotov et al. (2009), Izotov et al. (2011), Kehrig et al. (2004), Kehrig et al. (2011), Kennicutt & Skillman (2001), Kennicutt et al. (2003), Kinkel & Rosa (1994), Kniazev et al. (2000), Kobulnicky et al. (1997), Kunth & Sargent (1983), Kwitter & Aller (1981), Lee et al. (2003a), Lee et al. (2003b), Lee et al. (2004), Lee et al. (2005), Lequeux et al. (1979), López-Sánchez et al. (2004), López-Sánchez et al. (2007), López-Sánchez & Esteban (2009), López-Sánchez et al. (2011), Luridiana et al. (2002), Magrini & Gonçalves (2009), McCall et al. (1985), Melbourne et al. (2004), Melnick et al. (1992), Miller (1996), Noeske et al. (2000), Pagel et al. (1980), Pagel et al. (1992), Pastoriza et al. (1993), Peimbert et al. (1986), Peña et al. (2007), Pérez-Montero et al. (2009), Popescu & Hopp (2000), Pustilnik et al. (2002), Pustilnik et al. (2003a), Pustilnik et al. (2003b), Pustilnik et al. (2005), Pustilnik et al. (2006), Rayo et al. (1982), Saviane et al. (2008), Sed-

Figure 16a shows the excitation parameter P as a function of R_{23}. Excitation increases upwards, but R_{23} is double-valued with metallicity, so metallicity increases to the left for objects on the upper branch (the majority of the galaxies and stacks) and increases to the right for objects on the lower branch (most of the compiled H II regions). Figure 16b displays another projection of the same data in the space defined by the dereddened [O II] λ3727 and [O III] λ5007 line fluxes relative to Hβ. The dotted lines show constant R_{23} values, and the dashed lines mark constant [O II] λ3727/[O III] λ5007 values.

In Figure 16, the compiled H II regions predominantly overlap with the high excitation and high R_{23} tail of the galaxy distribution in Figure 16a and the analogous high [O III] λ5007 tail of the galaxy distribution in Figure 16b, which corresponds to low metallicity galaxies. The compiled H II regions have direct method metallicities and therefore at least one detectable auroral line, usually [O III] λ4363. Because the strength of the auroral lines, especially [O III] λ4363, is a strong function of metallicity and excitation parameter, these H II regions were effectively selected to have low metallicities and high excitation parameters. Thus, they are not representative of the typical conditions found in the H II regions of the galaxy sample. Empirical calibrations, which are based on samples of H II regions with direct method metallicities, are not well constrained in the high metallicity, low excitation regime where most galaxies and their constituent H II regions lie. For example, Moustakas et al. (2010) recommended only using the empirical Pilyugin & Thuan (2005) R_{23} calibration for objects with $P > 0.4$. When empirical calibrations are

wick & Aller (1981), Skillman (1985), Skillman & Kennicutt (1993), Skillman et al. (2003), Stanghellini et al. (2010), Terlevich et al. (1991), Thuan et al. (1995), Thuan et al. (1999), Torres-Peimbert et al. (1989), Tüllmann et al. (2003), van Zee et al. (1997), van Zee et al. (1998), van Zee (2000), van Zee & Haynes (2006), van Zee et al. (2006), Vilchez et al. (1988), Vílchez & Iglesias-Páramo (2003), Webster & Smith (1983), and Zahid & Bresolin (2011).

applied to large galaxy samples, galaxy metallicities are systematically underestimated, particularly at low excitation and high metallicity (Moustakas et al. 2010). Similarly, MZRs based on empirical calibrations may have an artificially weak dependence on SFR.

The typical excitation conditions and R_{23} values of the stacks are much better matched to the overall galaxy distribution than the compiled H II regions with direct method metallicities. The stacks probe to both lower excitation ($P \approx 0.2$) and higher metallicity ($R_{23} \approx 0.4$) than the bulk of the compiled H II regions. The stacks do not continue to low R_{23} values (<0.3), a region of parameter space populated by the most massive and metal-rich galaxies in our sample. The [O II] $\lambda 3727$ and [O III] $\lambda 5007$ line fluxes of these galaxies vary significantly, even at the same stellar mass and SFR. While the stacks do not reach the lowest R_{23} values of the galaxies, they still trace the average R_{23} values of the galaxies in each stack.

Theoretical calibrations are based on stellar population synthesis models, like STARBURST99 (Leitherer et al. 1999), and photoionization models, such as MAPPINGS (Sutherland & Dopita 1993; Groves et al. 2004a,b) and CLOUDY (Ferland et al. 1998). The stellar population synthesis model generates an ionizing radiation field that is then processed through the gas by the photoionization model. The parameters in the stellar population synthesis model include stellar metallicity, age of the ionizing source, initial mass function, and star formation history. In the photoionization model, the electron density and the ionization parameter are adjustable parameters. Because the model grids can span a wide range of parameter space, particularly in metallicity and excitation parameter, theoretical calibrations have an advantage over empirical calibrations at high metallicity and low excitation, where empirical calibrations are not strictly applicable.

However, metallicities derived with theoretical calibrations can be significantly higher (up to 0.7 dex; see Kewley & Ellison 2008) than direct method metallicities. The most likely cause of this offset is the breakdown of one or more of the assumptions about the physics of H II regions in the stellar population synthesis or photoionization models. In the stellar population synthesis models, the ionizing source is usually treated as a zero age main sequence starburst, which is not applicable for older star clusters (Berg et al. 2011), and the line fluxes can change appreciably as a cluster (and the associated H II region) ages. As elucidated by Kewley & Ellison (2008), there are three main issues with the photoionization models. First, they treat the nebular geometry as either spherical or plane-parallel, which may not be appropriate for the true geometries of the H II regions. Second, the fraction of metals depleted onto dust grains is poorly constrained by observations (see Draine 2003; Jenkins 2009) but is a required parameter of the photoionization models. Third, they assume that the density distribution of the gas and dust as smooth, when it is clumpy. While all these assumptions might break down to some degree, it is unknown which assumption or assumptions causes metallicities based on theoretical strong line calibrations to be offset from the direct method metallicities, but it is conceivable that the weak SFR dependence of theoretical strong line calibration MZRs is also due to these assumptions.

One of the most intriguing findings of the Mannucci et al. (2010) and Lara-López et al. (2010) studies is that high redshift observations are consistent with no redshift evolution of the strong line FMR up to $z = 2.5$ and $z = 3.5$, respectively.

Given the large discrepancies between the local strong line and direct method FMRs, a fair comparison between the local direct method FMR and a high redshift strong line FMR is not possible. An interesting test would be to check if high redshift direct method metallicity measurements are consistent with the local direct method FMR. A few studies (Hoyos et al. 2005; Kakazu et al. 2007; Yuan & Kewley 2009; Erb et al. 2010; Brammer et al. 2012) have reported direct method metallicities at higher redshifts ($z \sim 0.7$–2.3), but none simultaneously provide the stellar masses and SFRs of the galaxies. Since the FMR and its evolution provide important constraints on theoretical galaxy evolution models and form the basis of empirical galaxy evolution models (Zahid et al. 2012b; Peeples & Somerville 2012), future studies that measure all three of these parameters would be valuable.

7.4. Physical Processes Governing the MZR and $M_\star$–Z–SFR Relation

Understanding the baryon cycling of galaxies relies heavily on the adopted relations between stellar mass, metallicity, and SFR. Traditionally, the MZR and $M_\star$–Z–SFR relation have been measured with strong line methods. In this study, we have used the more reliable direct method to measure the MZR and $M_\star$–Z–SFR relation. The direct method MZR (Figure 10) spans three orders of magnitude in stellar mass from $\log(M_\star) = 7.4$–10.5 and thus simultaneously extends the MZR to lower masses by an order of magnitude compared to strong line MZRs (e.g., T04) and resolves the high mass turnover. The features of the direct method MZR that most strongly influence the physical interpretations are its low mass slope (O/H $\propto M_\star^{1/2}$), its turnover mass ($\log[M_\star] = 8.9$), and its normalization ($12 + \log(\text{O/H})_{\text{asm}} = 8.8$). The SFR-dependence of the MZR (see Figures 11 and 12) also serves as an important observational constraint for galaxy evolution models. We find that the MZR depends strongly on SFR ($\alpha = 0.66$; Figure 12) at all stellar masses.

The MZR and $M_\star$–Z–SFR relation are shaped by gas inflows, gas outflows, and star formation. The interplay between these three processes is complex, so hydrodynamic galaxy simulations (e.g., Brooks et al. 2007; Finlator & Davé 2008; Davé et al. 2011b; Davé et al. 2011a) and analytic models (e.g., Peeples & Shankar 2011; Davé et al. 2012) have been used to establish a framework to interpret the observations in a physical context. Below we briefly discuss the physical implications of our results within the formalisms of Peeples & Shankar (2011) and Finlator & Davé (2008).

Peeples & Shankar (2011) developed an analytic model for understanding the importance of outflows in governing the MZR based on the assumption that galaxies follow zero scatter relations between stellar mass, gas fraction, metallicity, outflow efficiency, and host halo properties. In their formalism, the primary variable controlling the MZR is the metallicity-weighted mass-loading parameter,

$$\zeta_{\text{wind}} \equiv \left(\frac{Z_{\text{wind}}}{Z_{\text{ISM}}} \right) \left(\frac{\dot{M}_{\text{wind}}}{\dot{M}_\star} \right), \qquad (6)$$

where Z_{wind} and Z_{ISM} are the wind and ISM metallicities, respectively, and $\dot{M}_{\text{wind}}/\dot{M}_\star$ is the unweighted mass-loading parameter. ζ_{wind} can be expressed in terms of the MZR and the stellar mass–gas fraction relation by rearranging their Equation (20):

$$\zeta_{\text{wind}} = y/Z_{\text{ISM}} - 1 - \alpha F_{\text{gas}}, \qquad (7)$$

where y is the nucleosynthetic yield, α is a parameter of order unity (see their Equation 11), and $F_{\rm gas} \equiv M_{\rm gas}/M_\star$ is the gas fraction.

If we adopt the Peeples & Shankar (2011) formalism and their fiducial yield and stellar mass–gas fraction relation, then we can solve for the $M_\star$–$\zeta_{\rm wind}$ relation implied by the direct method MZR. This direct method $M_\star$–$\zeta_{\rm wind}$ relation starts at high $\zeta_{\rm wind}$ ($\zeta_{\rm wind} \sim 15$) for low mass galaxies ($\log[M_\star] = 7.5$). Then, $\zeta_{\rm wind}$ decreases with increasing stellar mass, eventually flattening and approaching a constant $\zeta_{\rm wind}$ ($\zeta_{\rm wind} \sim 2$) above the turnover mass ($\log[M_\star] = 8.9$). Since the D02 MZR has a similar shape and normalization to the direct method MZR from $\log(M_\star) = 8.5$–10.5, the direct method $M_\star$–$\zeta_{\rm wind}$ relation resembles the D02 $M_\star$–$\zeta_{\rm wind}$ relation shown in Figure 6 of Peeples & Shankar (2011). Also, the direct method MZR implies a similar behavior for $Z_{\rm wind}$ and $Z_{\rm ISM}$ as a function of stellar mass as the D02 MZR (see their Figure 9). The ratio of $Z_{\rm wind}/Z_{\rm ISM}$ inversely correlates with how efficiently winds entrain ambient ISM. If we adopt the simple relation between metallicity and the unweighted mass-loading parameter from Finlator & Davé (2008), $Z_{\rm ISM} \approx y/(1 + \dot{M}_{\rm wind}/\dot{M}_\star)$, then the direct method MZR implies an efficiency of mass ejection that scales as $\dot{M}_{\rm wind}/\dot{M}_\star \propto M_\star^{-1/2}$ for $\log(M_\star) \lesssim 9.0$. The higher $\zeta_{\rm wind}$ for low mass galaxies relative to high mass galaxies could be due to more enriched winds (larger $Z_{\rm wind}/Z_{\rm ISM}$) or more efficient mass ejection by winds (larger $\dot{M}_{\rm wind}/\dot{M}_\star$) or both. Peeples & Shankar (2011) found that the $M_\star$–$\zeta_{\rm wind}$ relation follows the general shape of the direct method $M_\star$–$\zeta_{\rm wind}$ relation regardless of the input MZR (see their Figure 6). However, the direct method MZR requires more efficient metal ejection by winds than theoretical strong line calibration MZRs (T04; Z94; KK04; M91) at all stellar masses because of the lower normalization of the direct method MZR. We note that the yield is poorly constrained, and a higher adopted yield requires more efficient outflows to produce the observed MZR.

In contrast to the Peeples & Shankar (2011) framework that assumed a zero scatter MZR (and therefore does not account for variations in the SFR or gas fraction at a fixed stellar mass), the Finlator & Davé (2008) model, based on cosmological hydrodynamic simulations, treats the MZR as an equilibrium condition. In their model, galaxies are perturbed off the MZR by stochastic inflows but the star formation triggered by the inflow of gas and the subsequent metal production returns them to the mean MZR. The rate at which galaxies re-equilibrate following an episode of gas inflow sets the scatter in the MZR, which is indirectly traced by the SFR-dependence of the $M_\star$–Z–SFR relation.

The observed SFR-dependence of the $M_\star$–Z–SFR relation differs according to the strong line metallicity calibration used to construct the $M_\star$–Z–SFR relation, as found by Yates et al. (2012). Specifically, they used metallicities estimated with the Mannucci et al. (2010) method and T04 method. At low stellar masses, metallicity decreases with increasing SFR for both $M_\star$–Z–SFR relations. But at high stellar masses ($\log[M_\star] \gtrsim 10.5$), the SFR-dependence of the T04 $M_\star$–Z–SFR relation reverses, so that metallicity increases with increasing SFR; however, the Mannucci et al. (2010) $M_\star$–Z–SFR relation collapses to a single sequence that is independent of SFR. Yates et al. (2012) suggested that the SFR-dependence of the Mannucci et al. (2010) $M_\star$–Z–SFR relation at high stellar mass is obscured by the N2 indicator (which was averaged with the metallicity estimated from R_{23}) used in the Mannucci et al.

(2010) metallicity calibration, which saturates at high metallicity.

Unlike the Mannucci et al. (2010) and T04 $M_\star$–Z–SFR relations, the SFR-dependence of the direct method $M_\star$–Z–SFR relation does not change dramatically with stellar mass. There is little overlap between the constant SFR tracks in the direct method $M_\star$–Z–SFR relation (Figure 11). Furthermore, the SFR-dependence is strong ($\alpha = 0.66$; see Section 5.3), so the scatter in the direct method MZR for individual galaxies (if it could be measured) would be larger than the scatter in the Mannucci et al. (2010) and T04 MZRs. Within the context of the Finlator & Davé (2008) model, this means that the direct method MZR implies a longer timescale for galaxies to re-equilibrate than the Mannucci et al. (2010) and T04 MZRs. We note that the direct method $M_\star$–Z–SFR relation does not probe above $\log(M_\star) = 10.5$ because the auroral lines are undetected in this regime; however, this mass scale is where the discrepancies between the Mannucci et al. (2010) and T04 metallicities are the largest—potentially due to a break down of strong line calibrations at high metallicities (see Section 7.3).

8. SUMMARY

We have measured [O III], [O II], [N II], and [S II] electron temperatures, direct method gas-phase oxygen abundances, and direct method gas-phase nitrogen to oxygen abundance ratios from stacked galaxy spectra. We stacked the spectra of $\sim$200,000 SDSS star-forming galaxies in bins of (1) 0.1 dex in stellar mass and (2) 0.1 dex in stellar mass and 0.5 dex in SFR. The high SNR stacked spectra enabled the detection of the temperature-sensitive auroral lines that are essential for metallicity measurements with the direct method. Auroral lines are weak, especially in massive, metal-rich objects, but we detect [O III] $\lambda 4363$ up to $\log(M_\star) = 9.4$ and [O II] $\lambda\lambda 7320$, 7330 up to $\log(M_\star) = 10.5$, which is generally not feasible for spectra of individual galaxies. We used the auroral line fluxes to derive the [O III] and [O II] electron temperatures, the O^{++} and O^+ ionic abundances, and the total oxygen abundances of the stacks.

We constructed the direct method mass–metallicity and $M_\star$–Z–SFR relations across a wide range of stellar mass ($\log[M_\star] = 7.4$–10.5) and SFR ($\log[\rm SFR] = -1.0 \rightarrow 2.0$). The direct method MZR rises steeply (O/H $\propto M_\star^{1/2}$) from $\log(M_\star) = 7.4$–8.9. The direct method MZR turns over at $\log(M_\star) = 8.9$, in contrast to strong line MZRs that typically turn over at higher masses ($\log[M_\star] \sim 10.5$). Above the turnover, the direct method MZR approaches an asymptotic metallicity of $12 + \log(\rm O/H) = 8.8$, which is consistent with empirical strong line calibration MZRs but $\sim$0.3 dex lower than theoretical strong line calibration MZRs like the Tremonti et al. (2004) MZR. Furthermore, we found that the SFR-dependence (as measured by the value of α that minimizes the scatter at fixed $\mu_\alpha \equiv \log(M_\star) - \alpha \log(\rm SFR)$ in the fundamental metallicity relation; see Equation 1) of the direct method $M_\star$–Z–SFR relation is $\sim$2–3 times larger ($\alpha = 0.66$) than for strong line $M_\star$–Z–SFR relations ($\alpha \sim 0.12$–0.34). Its SFR-dependence is monotonic as a function of stellar mass, so constant SFR tracks do not overlap, unlike strong line $M_\star$–Z–SFR relations.

We also showed that the direct method N/O relative abundance correlates strongly with oxygen abundance and even more strongly with stellar mass. N/O exhibits a clear transition from primary to secondary nitrogen enrichment as a function of oxygen abundance and stellar mass.

The slope, turnover, normalization, and SFR-dependence of the MZR act as critical constraints on galaxy evolution models and are best measured by methods that do not rely on strong line diagnostics, such as the direct method. Future work should aim to construct a direct method MZR of individual galaxies with high SNR optical spectra that enable the detection of auroral lines in high mass and high metallicity objects. Furthermore, metallicities based on *Herschel* observations of far-IR fine-structure lines will provide a valuable check on the absolute abundance scale, which is a major outstanding uncertainty for galaxy evolution studies. These types of investigations will improve our understanding of the galaxy formation process, particularly the cycling of baryons between galaxies and the IGM.

REFERENCES

Abazajian, K., et al. 2003, AJ, 126, 2081
Abazajian, K. N., et al. 2009, ApJS, 182, 543
Adelman-McCarthy, J. K., et al. 2008, ApJS, 175, 297
Berg, D. A., Skillman, E. D., & Marble, A. R. 2011, ApJ, 738, 2
Berg, D. A., et al. 2012, ArXiv e-prints
Brammer, G. B., et al. 2012, ApJ, 758, L17
Bresolin, F. 2007, ApJ, 656, 186
Bresolin, F. 2008, in The Metal-Rich Universe, ed. G. Israelian & G. Meynet, 155
Bresolin, F., Garnett, D. R., & Kennicutt, Jr., R. C. 2004, ApJ, 615, 228
Bresolin, F., Gieren, W., Kudritzki, R.-P., Pietrzyński, G., Urbaneja, M. A., & Carraro, G. 2009a, ApJ, 700, 309
Bresolin, F., Ryan-Weber, E., Kennicutt, R. C., & Goddard, Q. 2009b, ApJ, 695, 580
Bresolin, F., Schaerer, D., González Delgado, R. M., & Stasińska, G. 2005, A&A, 441, 981
Brinchmann, J., Charlot, S., White, S. D. M., Tremonti, C., Kauffmann, G., Heckman, T., & Brinkmann, J. 2004, MNRAS, 351, 1151
Brooks, A. M., Governato, F., Booth, C. M., Willman, B., Gardner, J. P., Wadsley, J., Stinson, G., & Quinn, T. 2007, ApJ, 655, L17
Bruzual, G., & Charlot, S. 2003, MNRAS, 344, 1000
Cai, W., & Pradhan, A. K. 1993, ApJS, 88, 329
Campbell, A., Terlevich, R., & Melnick, J. 1986, MNRAS, 223, 811
Cardelli, J. A., Clayton, G. C., & Mathis, J. S. 1989, ApJ, 345, 245
Castellanos, M., Díaz, A. I., & Terlevich, E. 2002, MNRAS, 329, 315
Cid Fernandes, R., Mateus, A., Sodré, L., Stasińska, G., & Gomes, J. M. 2005, MNRAS, 358, 363
Cresci, G., Mannucci, F., Sommariva, V., Maiolino, R., Marconi, A., & Brusa, M. 2012, MNRAS, 421, 262
Davé, R., Finlator, K., & Oppenheimer, B. D. 2011a, MNRAS, 416, 1354
—. 2012, MNRAS, 421, 98
Davé, R., Oppenheimer, B. D., & Finlator, K. 2011b, MNRAS, 415, 11
de Blok, W. J. G., & van der Hulst, J. M. 1998, A&A, 335, 421
De Robertis, M. M., Dufour, R. J., & Hunt, R. W. 1987, JRASC, 81, 195
Dekel, A., & Silk, J. 1986, ApJ, 303, 39
Dekel, A., & Woo, J. 2003, MNRAS, 344, 1131
Delahaye, F., & Pinsonneault, M. H. 2006, ApJ, 649, 529
Denicoló, G., Terlevich, R., & Terlevich, E. 2002, MNRAS, 330, 69
Draine, B. T. 2003, ARA&A, 41, 241
Ellison, S. L., Patton, D. R., Simard, L., & McConnachie, A. W. 2008, ApJ, 672, L107
Erb, D. K., Pettini, M., Shapley, A. E., Steidel, C. C., Law, D. R., & Reddy, N. A. 2010, ApJ, 719, 1168
Erb, D. K., Shapley, A. E., Pettini, M., Steidel, C. C., Reddy, N. A., & Adelberger, K. L. 2006, ApJ, 644, 813
Esteban, C., Bresolin, F., Peimbert, M., García-Rojas, J., Peimbert, A., & Mesa-Delgado, A. 2009, ApJ, 700, 654
Ferland, G. J., Korista, K. T., Verner, D. A., Ferguson, J. W., Kingdon, J. B., & Verner, E. M. 1998, PASP, 110, 761
Fierro, J., Torres-Peimbert, S., & Peimbert, M. 1986, PASP, 98, 1032
Finlator, K., & Davé, R. 2008, MNRAS, 385, 2181
French, H. B. 1980, ApJ, 240, 41
Fricke, K. J., Izotov, Y. I., Papaderos, P., Guseva, N. G., & Thuan, T. X. 2001, AJ, 121, 169
García-Rojas, J., & Esteban, C. 2007, ApJ, 670, 457
Garnett, D. R. 1990, ApJ, 363, 142
—. 1992, AJ, 103, 1330
—. 2002, ApJ, 581, 1019
Garnett, D. R., Kennicutt, Jr., R. C., & Bresolin, F. 2004, ApJ, 607, L21
Garnett, D. R., Shields, G. A., Skillman, E. D., Sagan, S. P., & Dufour, R. J. 1997, ApJ, 489, 63
Gonzalez-Delgado, R. M., et al. 1994, ApJ, 437, 239
Groves, B. A., Dopita, M. A., & Sutherland, R. S. 2004a, ApJS, 153, 9
—. 2004b, ApJS, 153, 75
Guseva, N. G., Izotov, Y. I., Stasińska, G., Fricke, K. J., Henkel, C., & Papaderos, P. 2011, A&A, 529, A149
Guseva, N. G., Izotov, Y. I., & Thuan, T. X. 2000, ApJ, 531, 776
Guseva, N. G., Papaderos, P., Izotov, Y. I., Green, R. F., Fricke, K. J., Thuan, T. X., & Noeske, K. G. 2003a, A&A, 407, 91
—. 2003b, A&A, 407, 105
Guseva, N. G., Papaderos, P., Izotov, Y. I., Noeske, K. G., & Fricke, K. J. 2004, A&A, 421, 519
Guseva, N. G., Papaderos, P., Meyer, H. T., Izotov, Y. I., & Fricke, K. J. 2009, A&A, 505, 63
Guseva, N. G., et al. 2001, A&A, 378, 756
Hägele, G. F., Díaz, Á. I., Terlevich, E., Terlevich, R., Pérez-Montero, E., & Cardaci, M. V. 2008, MNRAS, 383, 209
Hawley, S. A. 1978, ApJ, 224, 417
Henry, R. B. C., Edmunds, M. G., & Köppen, J. 2000, ApJ, 541, 660
Hodge, P., & Miller, B. W. 1995, ApJ, 451, 176
Hoyos, C., Koo, D. C., Phillips, A. C., Willmer, C. N. A., & Guhathakurta, P. 2005, ApJ, 635, L21
Izotov, Y. I., Chaffee, F. H., Foltz, C. B., Green, R. F., Guseva, N. G., & Thuan, T. X. 1999, ApJ, 527, 757
Izotov, Y. I., Chaffee, F. H., & Green, R. F. 2001, ApJ, 562, 727
Izotov, Y. I., Guseva, N. G., Fricke, K. J., & Henkel, C. 2011, A&A, 533, A25
Izotov, Y. I., Guseva, N. G., Fricke, K. J., & Papaderos, P. 2009, A&A, 503, 61

Izotov, Y. I., Papaderos, P., Guseva, N. G., Fricke, K. J., & Thuan, T. X. 2004, A&A, 421, 539

Izotov, Y. I., Stasińska, G., Meynet, G., Guseva, N. G., & Thuan, T. X. 2006, A&A, 448, 955

Izotov, Y. I., & Thuan, T. X. 1998a, ApJ, 497, 227

—. 1998b, ApJ, 500, 188

—. 2004, ApJ, 602, 200

Izotov, Y. I., Thuan, T. X., & Lipovetsky, V. A. 1994, ApJ, 435, 647

—. 1997, ApJS, 108, 1

Jenkins, E. B. 2009, ApJ, 700, 1299

Kakazu, Y., Cowie, L. L., & Hu, E. M. 2007, ApJ, 668, 853

Kauffmann, G., et al. 2003a, MNRAS, 341, 33

—. 2003b, MNRAS, 346, 1055

Kehrig, C., Telles, E., & Cuisinier, F. 2004, AJ, 128, 1141

Kehrig, C., et al. 2011, A&A, 526, A128

Kennicutt, Jr., R. C., Bresolin, F., French, H., & Martin, P. 2000, ApJ, 537, 589

Kennicutt, Jr., R. C., Bresolin, F., & Garnett, D. R. 2003, ApJ, 591, 801

Kennicutt, Jr., R. C., & Skillman, E. D. 2001, AJ, 121, 1461

Kewley, L. J., & Dopita, M. A. 2002, ApJS, 142, 35

Kewley, L. J., & Ellison, S. L. 2008, ApJ, 681, 1183

Kewley, L. J., Geller, M. J., & Barton, E. J. 2006, AJ, 131, 2004

Kewley, L. J., Jansen, R. A., & Geller, M. J. 2005, PASP, 117, 227

Kewley, L. J., Rupke, D., Zahid, H. J., Geller, M. J., & Barton, E. J. 2010, ApJ, 721, L48

Khan, R., Stanek, K. Z., Stoll, R., & Prieto, J. L. 2011, ApJ, 737, L24

Kinkel, U., & Rosa, M. R. 1994, A&A, 282, L37

Kniazev, A. Y., et al. 2000, A&A, 357, 101

Kobulnicky, H. A., Kennicutt, Jr., R. C., & Pizagno, J. L. 1999, ApJ, 514, 544

Kobulnicky, H. A., & Kewley, L. J. 2004, ApJ, 617, 240

Kobulnicky, H. A., & Skillman, E. D. 1997, ApJ, 489, 636

Kobulnicky, H. A., Skillman, E. D., Roy, J.-R., Walsh, J. R., & Rosa, M. R. 1997, ApJ, 477, 679

Kriss, G. 1994, Astronomical Data Analysis Software and Systems, 3, 437

Kunth, D., & Sargent, W. L. W. 1983, ApJ, 273, 81

Kwitter, K. B., & Aller, L. H. 1981, MNRAS, 195, 939

Lara-López, M. A., et al. 2010, A&A, 521, L53

Le Borgne, J.-F., et al. 2003, A&A, 402, 433

Lee, H., Grebel, E. K., & Hodge, P. W. 2003a, A&A, 401, 141

Lee, H., McCall, M. L., & Richer, M. G. 2003b, AJ, 125, 2975

Lee, H., Skillman, E. D., Cannon, J. M., Jackson, D. C., Gehrz, R. D., Polomski, E. F., & Woodward, C. E. 2006, ApJ, 647, 970

Lee, H., Skillman, E. D., & Venn, K. A. 2005, ApJ, 620, 223

Lee, J. C., Salzer, J. J., & Melbourne, J. 2004, ApJ, 616, 752

Leitherer, C., et al. 1999, ApJS, 123, 3

Lequeux, J., Peimbert, M., Rayo, J. F., Serrano, A., & Torres-Peimbert, S. 1979, A&A, 80, 155

Liang, Y. C., Hammer, F., Yin, S. Y., Flores, H., Rodrigues, M., & Yang, Y. B. 2007, A&A, 473, 411

Liu, X.-W., Storey, P. J., Barlow, M. J., Danziger, I. J., Cohen, M., & Bryce, M. 2000, MNRAS, 312, 585

López-Sánchez, A. R., & Esteban, C. 2009, A&A, 508, 615

López-Sánchez, Á. R., Esteban, C., García-Rojas, J., Peimbert, M., & Rodríguez, M. 2007, ApJ, 656, 168

López-Sánchez, Á. R., Esteban, C., & Rodríguez, M. 2004, ApJS, 153, 243

López-Sánchez, Á. R., Mesa-Delgado, A., López-Martín, L., & Esteban, C. 2011, MNRAS, 411, 2076

Luridiana, V., Esteban, C., Peimbert, M., & Peimbert, A. 2002, Rev. Mex. Astron. Astrofis, 38, 97

Magrini, L., & Gonçalves, D. R. 2009, MNRAS, 398, 280

Maiolino, R., et al. 2008, A&A, 488, 463

Mannucci, F., Cresci, G., Maiolino, R., Marconi, A., & Gnerucci, A. 2010, MNRAS, 408, 2115

McCall, M. L., Rybski, P. M., & Shields, G. A. 1985, ApJS, 57, 1

McGaugh, S. S. 1991, ApJ, 380, 140

Melbourne, J., Phillips, A., Salzer, J. J., Gronwall, C., & Sarajedini, V. L. 2004, AJ, 127, 686

Melnick, J., Heydari-Malayeri, M., & Leisy, P. 1992, A&A, 253, 16

Miller, B. W. 1996, AJ, 112, 991

Moustakas, J., & Kennicutt, Jr., R. C. 2006, ApJ, 651, 155

Moustakas, J., Kennicutt, Jr., R. C., Tremonti, C. A., Dale, D. A., Smith, J.-D. T., & Calzetti, D. 2010, ApJS, 190, 233

Moustakas, J., et al. 2011, arXiv:1112.3300

Murray, N., Quataert, E., & Thompson, T. A. 2005, ApJ, 618, 569

Nava, A., Casebeer, D., Henry, R. B. C., & Jevremovic, D. 2006, ApJ, 645, 1076

Nicholls, D. C., Dopita, M. A., & Sutherland, R. S. 2012, ApJ, 752, 148

Noeske, K. G., Guseva, N. G., Fricke, K. J., Izotov, Y. I., Papaderos, P., & Thuan, T. X. 2000, A&A, 361, 33

Oppenheimer, B. D., & Davé, R. 2006, MNRAS, 373, 1265

Osterbrock, D. E. 1989, Astrophysics of gaseous nebulae and active galactic nuclei, ed. Osterbrock, D. E.

Pagel, B. E. J., Edmunds, M. G., & Smith, G. 1980, MNRAS, 193, 219

Pagel, B. E. J., Simonson, E. A., Terlevich, R. J., & Edmunds, M. G. 1992, MNRAS, 255, 325

Pastoriza, M. G., Dottori, H. A., Terlevich, E., Terlevich, R., & Diaz, A. I. 1993, MNRAS, 260, 177

Peña, M., Stasińska, G., & Richer, M. G. 2007, A&A, 476, 745

Peeples, M. S., Pogge, R. W., & Stanek, K. Z. 2009, ApJ, 695, 259

Peeples, M. S., & Shankar, F. 2011, MNRAS, 417, 2962

Peeples, M. S., & Somerville, R. 2012, ArXiv e-prints

Peimbert, M. 1967, ApJ, 150, 825

Peimbert, M., & Costero, R. 1969, Boletin de los Observatorios Tonantzintla y Tacubaya, 5, 3

Peimbert, M., Pena, M., & Torres-Peimbert, S. 1986, A&A, 158, 266

Pérez-Montero, E., & Contini, T. 2009, MNRAS, 398, 949

Pérez-Montero, E., García-Benito, R., Díaz, A. I., Pérez, E., & Kehrig, C. 2009, A&A, 497, 53

Perez-Montero, E., et al. 2012, arXiv:1210.0334

Pettini, M., & Pagel, B. E. J. 2004, MNRAS, 348, L59

Pilyugin, L. S., Grebel, E. K., & Mattsson, L. 2012, MNRAS, 424, 2316

Pilyugin, L. S., & Thuan, T. X. 2005, ApJ, 631, 231

Pilyugin, L. S., Vílchez, J. M., Cedrés, B., & Thuan, T. X. 2010, MNRAS, 403, 896

Pilyugin, L. S., Vílchez, J. M., & Thuan, T. X. 2006, MNRAS, 370, 1928

Popescu, C. C., & Hopp, U. 2000, A&AS, 142, 247

Pustilnik, S., Zasov, A., Kniazev, A., Pramskij, A., Ugryumov, A., & Burenkov, A. 2003a, A&A, 400, 841

Pustilnik, S. A., Engels, D., Kniazev, A. Y., Pramskij, A. G., Ugryumov, A. V., & Hagen, H.-J. 2006, Astronomy Letters, 32, 228

Pustilnik, S. A., Kniazev, A. Y., Masegosa, J., Márquez, I. M., Pramskij, A. G., & Ugryumov, A. V. 2002, A&A, 389, 779

Pustilnik, S. A., Kniazev, A. Y., & Pramskij, A. G. 2005, A&A, 443, 91

Pustilnik, S. A., Kniazev, A. Y., Pramskij, A. G., Ugryumov, A. V., & Masegosa, J. 2003b, A&A, 409, 917

Rayo, J. F., Peimbert, M., & Torres-Peimbert, S. 1982, ApJ, 255, 1

Richard, J., Jones, T., Ellis, R., Stark, D. P., Livermore, R., & Swinbank, M. 2011, MNRAS, 413, 643

Rubin, V. C., Ford, Jr., W. K., & Whitmore, B. C. 1984, ApJ, 281, L21

Sánchez-Blázquez, P., et al. 2006, MNRAS, 371, 703

Saviane, I., Ivanov, V. D., Held, E. V., Alloin, D., Rich, R. M., Bresolin, F., & Rizzi, L. 2008, A&A, 487, 901

Schlegel, D. J., Finkbeiner, D. P., & Davis, M. 1998, ApJ, 500, 525

Searle, L. 1971, ApJ, 168, 327

Sedwick, K. E., & Aller, L. H. 1981, Proceedings of the National Academy of Science, 78, 1994

Shaw, R. A., & Dufour, R. J. 1995, PASP, 107, 896

Skillman, E. D. 1985, ApJ, 290, 449

Skillman, E. D., Côté, S., & Miller, B. W. 2003, AJ, 125, 610

Skillman, E. D., & Kennicutt, Jr., R. C. 1993, ApJ, 411, 655

Stanek, K. Z., et al. 2006, Acta Astron., 56, 333

Stanghellini, L., Magrini, L., Villaver, E., & Galli, D. 2010, A&A, 521, A3

Stasińska, G. 1982, A&AS, 48, 299

—. 2005, A&A, 434, 507

Stasińska, G. 2010, in IAU Symposium, Vol. 262, IAU Symposium, ed. G. Bruzual & S. Charlot, 93–96

Stoll, R., Prieto, J. L., Stanek, K. Z., Pogge, R. W., Szczygieł, D. M., Pojmański, G., Antognini, J., & Yan, H. 2011, ApJ, 730, 34

Stoughton, C., et al. 2002, AJ, 123, 485

Strauss, M. A., et al. 2002, AJ, 124, 1810

Sutherland, R. S., & Dopita, M. A. 1993, ApJS, 88, 253

Terlevich, R., Melnick, J., Masegosa, J., Moles, M., & Copetti, M. V. F. 1991, A&AS, 91, 285

Thuan, T. X., Izotov, Y. I., & Foltz, C. B. 1999, ApJ, 525, 105

Thuan, T. X., Izotov, Y. I., & Lipovetsky, V. A. 1995, ApJ, 445, 108

Torres-Peimbert, S., Peimbert, M., & Fierro, J. 1989, ApJ, 345, 186

Torrey, P., Cox, T. J., Kewley, L., & Hernquist, L. 2012, ApJ, 746, 108

Tremonti, C. A., et al. 2004, ApJ, 613, 898

Tüllmann, R., Rosa, M. R., Elwert, T., Bomans, D. J., Ferguson, A. M. N., & Dettmar, R.-J. 2003, A&A, 412, 69

van Zee, L. 2000, ApJ, 543, L31

van Zee, L., & Haynes, M. P. 2006, ApJ, 636, 214
van Zee, L., Haynes, M. P., & Salzer, J. J. 1997, AJ, 114, 2479
van Zee, L., Salzer, J. J., Haynes, M. P., O'Donoghue, A. A., & Balonek, T. J. 1998, AJ, 116, 2805
van Zee, L., Skillman, E. D., & Haynes, M. P. 2006, ApJ, 637, 269
Vazdekis, A., Sánchez-Blázquez, P., Falcón-Barroso, J., Cenarro, A. J., Beasley, M. A., Cardiel, N., Gorgas, J., & Peletier, R. F. 2010, MNRAS, 404, 1639
Vila Costas, M. B., & Edmunds, M. G. 1993, MNRAS, 265, 199
Vílchez, J. M., & Iglesias-Páramo, J. 2003, ApJS, 145, 225
Vilchez, J. M., Pagel, B. E. J., Diaz, A. I., Terlevich, E., & Edmunds, M. G. 1988, MNRAS, 235, 633
Webster, B. L., & Smith, M. G. 1983, MNRAS, 204, 743
Wright, E. L. 2006, PASP, 118, 1711
Yates, R. M., Kauffmann, G., & Guo, Q. 2012, MNRAS, 422, 215

Yin, S. Y., Liang, Y. C., Hammer, F., Brinchmann, J., Zhang, B., Deng, L. C., & Flores, H. 2007, A&A, 462, 535
York, D. G., et al. 2000, AJ, 120, 1579
Yuan, T.-T., & Kewley, L. J. 2009, ApJ, 699, L161
Zahid, H. J., & Bresolin, F. 2011, AJ, 141, 192
Zahid, H. J., Bresolin, F., Kewley, L. J., Coil, A. L., & Davé, R. 2012a, ApJ, 750, 120
Zahid, H. J., Dima, G. I., Kewley, L. J., Erb, D. K., & Davé, R. 2012b, ApJ, 757, 54
Zahid, H. J., Kewley, L. J., & Bresolin, F. 2011, ApJ, 730, 137
Zaritsky, D., Kennicutt, Jr., R. C., & Huchra, J. P. 1994, ApJ, 420, 87
Zhang, D., & Thompson, T. A. 2012, MNRAS, 424, 1170